

Nonstop Variability of Sgr A* Using JWST at 2.1 and 4.8 μ m Wavelengths: Evidence for Distinct Populations of Faint and Bright Variable Emission

F. Yusef-Zadeh¹ , H. Bushouse² , R. G. Arendt^{3,4,5} , M. Wardle⁶ , J. M. Michail^{7,8} , and C. J. Chandler⁹ 

¹ Department of Physics and Astronomy, CIERA, Northwestern University, 2145 Sheridan Road, Evanston, IL 60207, USA; zadeh@northwestern.edu

² Space Telescope Science Institute, 3700 San Martin Drive, Baltimore, MD 21218, USA; bushouse@stsci.edu

³ Center for Space Sciences and Technology, University of Maryland, Baltimore County, Baltimore, MD 21250, USA; Richard.G.Arendt@nasa.gov

⁴ Code 665, NASA/GSFC, 8800 Greenbelt Road, Greenbelt, MD 20771, USA

⁵ Center for Research and Exploration in Space Science and Technology, NASA/GSFC, Greenbelt, MD 20771, USA

⁶ School of Mathematical and Physical Sciences, Centre for Astronomy and Space Technology, Macquarie University, Sydney NSW 2109, Australia; mark.wardle@mq.edu.au

⁷ Center for Astrophysics, Harvard & Smithsonian, 60 Garden Street, Cambridge, MA 02138, USA; joseph.michail@cfa.harvard.edu

⁸ NSF Astronomy and Astrophysics Postdoctoral Fellow

⁹ National Radio Astronomy Observatory, P.O. Box O, Socorro, NM 87801, USA; chandle@nrao.edu

Received 2024 November 22; revised 2024 December 17; accepted 2024 December 18; published 2025 February 18

Abstract

We present the first results of JWST Cycle 1 and 2 observations of Sgr A* using NIRCam taken simultaneously at 2.1 and 4.8 μ m for a total of \sim 48 hr over seven different epochs in 2023 and 2024. We find correlated variability at 2.1 and 4.8 μ m in all epochs, continual short-timescale (a few seconds) variability, and epoch-to-epoch variable emission implying long-term (\sim days to months) variability of Sgr A*. A highlight of this analysis is the evidence for subminute, horizon-scale time variability of Sgr A*, probing inner accretion disk size scales. The power spectra of the light curves in each observing epoch also indicate long-term variable emission. With continuous observations, JWST data suggest that the flux of Sgr A* is fluctuating constantly. The flux density correlation exhibits a distinct break in the slope at \sim 3 mJy at 2.1 μ m. The analysis indicates two different processes contributing to the variability of Sgr A*. Brighter emission trends toward shallower spectral indices than the fainter emission. Cross-correlation of the light curves indicates for the first time a time delay of 3–40 s in the 4.8 μ m variability with respect to 2.1 μ m. This phase shift leads to loops in plots of flux density versus spectral index as the emission rises and falls. Modeling suggests that the synchrotron emission from the evolving, age-stratified electron population reproduces the shape of the observed light curves with a direct estimate of the magnetic field strengths in the range between 40 and 90 G and an upper cutoff energy, E_c , between 420 and 720 MeV.

Unified Astronomy Thesaurus concepts: Black hole physics (159)

1. Introduction

The center of our Galaxy hosts a $4 \times 10^6 M_\odot$ supermassive black hole, Sgr A*, presenting an unparalleled opportunity to study up close how material is irradiated, captured, accreted, and ejected by a black hole. The accretion disk of Sgr A* is fueled by winds from young, mass-losing stars orbiting within a few arcseconds (0.1 pc) of the black hole with yearly to decadal orbital timescales. The bolometric luminosity of Sgr A* is only \sim 100 L_\odot , suggesting that a small fraction of the infalling material reaches the event horizon (E. Quataert 2004; F. Yuan & R. Narayan 2014; Q. Wang & W. E. Moerner 2015). The exact nature of the accretion flow is still not well understood (F. Yuan et al. 2003; J. E. Goldston et al. 2005; M. Moscibrodzka & H. Falcke 2013; J. Dexter et al. 2020; S. M. Ressler et al. 2020a, 2020b, 2023).

Now that the size of the Sgr A* event horizon shadow silhouetted against its accretion disk, 51.8μ as, has been measured by the Event Horizon Telescope (Event Horizon Telescope Collaboration 2022), the focus is on the variability of the emission spanning from radio to X-ray wavelengths (R. Genzel & T. Ott 2003; F. Yusef-Zadeh et al. 2006; J. Neilsen et al. 2013; G. Witzel et al. 2021; M. Wielgus et al. 2022).

The variability of near-IR (NIR) emission is a key tracer of the dynamics of the inner accretion flow and the mechanisms at work within it (R. Genzel & T. Ott 2003; A. M. Ghez et al. 2005; F. Yusef-Zadeh et al. 2006; A. Eckart et al. 2008; J. M. Michail et al. 2021, 2024). When combined with other wavelengths, NIR probes the ejection, expansion, and orbital motion of material (hot spots) occurring near Sgr A*'s event horizon. NIR observations have revealed several bright, hourly timescale flaring events per day that are localized in the accretion flow to within a few gravitational radii (r_g ; T. Do et al. 2009). Projected orbits of hot spots in the accretion flow located within a few microarcseconds of Sgr A* have been determined on hourly timescales (GRAVITY Collaboration et al. 2018). GRAVITY measurements have also reported a hot-spot velocity of \sim 0.3c with an emitting region of \sim 5 r_g corresponding to 2.5 Schwarzschild radii (R_s ; the light travel time of 1 R_s is \sim 38 s; GRAVITY Collaboration et al. 2018, 2020).

The flux dependence of the spectral index α , where $\alpha \propto \log F_\nu / \log \nu$, has been studied in the past, but there is a debate on how the spectral index behaves at low flux densities. Steeper spectral indices at low flux densities have been reported (F. Eisenhauer et al. 2005; S. Gillessen et al. 2006; A. Krabbe et al. 2006; F. Yusef-Zadeh et al. 2006, 2009; M. Bremer et al. 2011; G. Ponti et al. 2017; G. Witzel et al. 2018), whereas some studies report that the spectral index is independent of



Original content from this work may be used under the terms of the [Creative Commons Attribution 4.0 licence](https://creativecommons.org/licenses/by/4.0/). Any further distribution of this work must maintain attribution to the author(s) and the title of the work, journal citation and DOI.

flux density (S. D. Hornstein et al. 2007; G. Trap et al. 2011; G. Witzel et al. 2014; H. Paugnat et al. 2024).

Long-term variability of faint flickering activity has also been reported, which provides global details of the accretion flow (G. C. Weldon et al. 2023). Thus, time variability analysis of Sgr A* provides details of compact spots with high plasma density and magnetic field strength but also large-scale flow in the accretion disk. Magnetohydrodynamic (MHD) simulations of the accretion flow predict flux variability on a wide range of timescales, from minutes to years (J. Dexter et al. 2020; S. M. Ressler et al. 2020a, 2020b; K. Chatterjee et al. 2021; G. C. Weldon et al. 2023).

There is a wealth of observations using mainly the Keck, Very Large Telescope, and Spitzer observatories, but also Hubble Space Telescope measurements, studying the physical characteristics of the variable emission at NIR wavelengths (F. Eisenhauer et al. 2005; A. M. Ghez et al. 2005; S. Gillessen et al. 2006; A. Krabbe et al. 2006; S. D. Hornstein et al. 2007; A. Eckart et al. 2008; K. Dodds-Eden et al. 2009; F. Yusef-Zadeh et al. 2009; M. Bremer et al. 2011; G. Trap et al. 2011; J. L. Hora et al. 2014; G. Witzel et al. 2014, 2018; E. Mossoux et al. 2016; G. Ponti et al. 2017; G. G. Fazio et al. 2018). Because of a large concentration of stellar sources in the Galactic center, there is considerable confusion in subtracting the background from the variable emission from Sgr A*. The complexity of the region in the immediate vicinity of Sgr A* has created debates on the flux distribution, power spectrum, spectral index, and periodicity of the emission. JWST observations have an advantage over ground-based adaptive optics instruments in observing for long, continuous periods and monitoring the spectral evolution of the variable emission through simultaneous observations at multiple wavelengths. Here we focus only on NIRCam 2.1 and 4.8 μm data presenting the results and analysis of the measurements. We then compare them with other measurements in the discussion.

In Section 2, we describe the observational details of seven epochs of observations in 2023 and 2024 followed by calibration and data processing. In Section 3.1, we show background subtraction, reference stars, and extinction-corrected light curves of Sgr A* in seven epochs separated by a few days, months, and a year. Our analysis indicates continuous short-timescale variability on seconds-to-hours and day-to-day variable emission implying no steady component of the emission from Sgr A*. We focus on the intrinsic short and long time variability associated with the hot-spot picture and the large-scale flow of the accretion disk, respectively. These are followed by modeling of the flux distribution at 2.1 and 4.8 μm . In Section 3.2, we fit the power spectrum on each epoch of observation and discuss two different statistics applied to low- and high-frequency variable emission. The histogram of intensities of the variable emission suggests a bimodal distribution with different statistics in the short- and long-term variability of Sgr A*. In Section 3.3, we concentrate on the time evolution of the spectral index of Sgr A* and show that the spectral index evolves differently at fainter and brighter flux densities. In Section 3.4, we present a cross-correlation analysis of 2.1 versus 4.8 μm emission. We note time delays of up to 40 s between 2.1 and 4.8 μm emission. We examine the flux density as a function of the spectral index and show loop diagrams indicating the evidence that the mean spectral index tends to steepen with increasing brightness up to ~ 3 mJy at 2.1 μm , without any further

steepening at higher brightnesses. In Section 4, we discuss models of the variable emission from Sgr A* and loop diagrams, giving estimates of the electron density and the magnetic field.

2. JWST NIRCam Observations

NIR photometric monitoring data of Sgr A* were obtained with the NIRCam instrument (M. J. Rieke et al. 2023) of JWST during 7 days from 2023 April through 2024 April. The observations were obtained under JWST Cycle 1 and 2 programs 2235 and 3559, respectively. All observations used the NIRCam instrument to acquire imaging of the region near Sgr A* using detectors in module B of the instrument. Simultaneous imaging was obtained in the NIRCam short- and long-wavelength channels using the medium-band filters F210M and F480M. These filters have central wavelengths of 2.096 and 4.814 μm , with bandwidths of 0.205 and 0.299 μm , respectively.

Two different observing methods were employed. All observations obtained in the 5 days of 2023 used conventional imaging of the field, employing a four-point dither pattern in order to avoid possible effects of detector persistence and to increase the effective sampling of the instrumental point-spread function (PSF). Based on analysis of the 2023 observations, it was determined that (1) persistence was not an issue, (2) dithering increased the risk of failing to reacquire the guide star after each move, and (3) more precise relative photometry could be obtained by not dithering. Hence, all observations obtained in 2024 used the NIRCam time series imaging method, where the source is left at a fixed location in the field and many individual images are obtained over the hours-long duration of the observation.

The observations obtained on 2023 April 13, 16, and 18 used the “SUB640” subarray detector readout, along with 10 groups (nondestructive detector readouts) per integration and 18 or 19 integrations per exposure. The 2023 September 22 observations also used the “SUB640” readout, with five groups per integration and 33 integrations per exposure. This results in images with an effective integration time of 41.9 s (same as in Table 1) and 951 s intervals between dither steps (see Table 1). The observations taken in time series mode in 2024 March and April used a somewhat smaller subarray readout (“SUB400P”), with 10 groups per integration, resulting in images with an effective integration time of 16.6 s. The total span of observations on 2023 April 13, 16, and 18 was ~ 7 hr; on 2023 September 22, it was ~ 5 hr; on 2024 March 22, it was ~ 6 hr; and on 2024 April 5 and 7, it was ~ 8.5 hr.

Columns (1)–(3) of Table 1 list the dates and the wavelengths that were used in all seven epochs of observations. The photon collection times of individual images used in the analysis are shown in column (5), whereas the cadence between subsequent images (which includes overheads and dead time) is shown in column (4). The last column shows the observing technique that was used in 2023 and 2024. For days 1–3, the total time spent taking multiple integrations within a single exposure before moving to a new dither point on the sky is ~ 795 s, while the cadence between successive exposures is ~ 954 s. For the last three epochs, where we used the time series mode without any dithering, there is no information for exposure cadence because all the data were taken as part of a single exposure.

Table 1
NIRCam Observation Dates

Epoch (1)	Date (2)	Wavelength (μm) (3)	Sampling Time (s) (4)	Exposure Time (s) (5)	Observing Technique (6)
Day 1	2023 Apr 13	2.1 and 4.8	46.066	41.89	Dither
Day 2	2023 Apr 16	2.1 and 4.8	46.066	41.89	Dither
Day 3	2023 Apr 18	2.1	46.066	41.89	Dither
Day 4	2023 Sep 22	2.1 and 4.8	25.135	20.93	Dither
Day 5	2024 Mar 21	2.1 and 4.8	18.241	16.56	Time series
Day 6	2024 Apr 5	2.1 and 4.8	18.241	16.56	Time series
Day 7	2024 Apr 7	2.1 and 4.8	18.241	16.56	Time series

Some problems were encountered with the observatory during the first three epochs, mainly due to the difficulty in finding and locking onto guide stars in this severely crowded region of the sky. In particular, the observations obtained on 2023 April 18 locked onto the wrong guide star, resulting in Sgr A* being just outside the field of view of the NIRCam long-wavelength channel. We therefore only have 2.1 μm data available on that day. In addition, the data obtained on 2023 April 16 showed evidence of poor guiding during some of the exposures, resulting in smeared images. Data from those exposures has been excluded from the analysis, resulting in some temporal gaps on that day. Finally, during the observations on 2023 September 22, the observatory lost the lock on the guide star about halfway through the planned observations, resulting in a truncation of the time coverage for that day.

2.1. JWST Data Processing and Analysis

The standard JWST calibration pipeline software and calibration reference files were still changing rapidly throughout 2023, so the data from all NIRCam observations of Sgr A* were uniformly reprocessed using the STScI pipeline from “*jwst*” package version 1.14, using the latest calibration reference files. All data sets were reprocessed from their raw form through Stages 1 and 2 of the pipeline, yielding fully recalibrated images from each individual integration in all exposures.

The absolute pointing accuracy of JWST is ~ 0.1 rms. In addition to this random uncertainty, some of the NIRCam observations misidentified the planned guide star, due to the extremely crowded nature of the Galactic center. This led to an even larger offset in pointing of several arcseconds for some exposures. Because Sgr A* is partially hidden by NIR diffuse background emission, as well as the overlapping PSFs of neighboring stars, accurate astrometric registration is needed in order to positively identify the exact position of Sgr A* in the images. We therefore used the highly accurate coordinates of several radio sources visible in a 230 GHz image of the Galactic center using the Atacama Large Millimeter/submillimeter Array (ALMA). The ALMA image is an average of the observations taken on 2023 August 25 and 2023 September 22, the latter of which was taken simultaneously with the day 4 (2023 September 22) NIRCam observations to astrometrically register the NIR images. There are a number of ALMA sources that have IR counterparts in the NIRCam images. The sky coordinates (R.A./decl.) of the radio sources were used as an absolute reference catalog to feed to the “*tweakreg*” task in the *jwst* pipeline package, which matches the locations of those sources in the NIRCam images and updates the World

Coordinate System (WCS) information in each image with the new absolute pointing information. This process could only be directly applied to the 2.1 μm NIRCam images, because the counterparts of the radio sources were all saturated in the 4.8 μm images. So the registration of the 4.8 μm images was accomplished by bootstrapping source positions from the already-registered 2.1 μm images using the same “*tweakwcs*” task. This process was used to astrometrically register all NIRCam data from the 2023–2024 campaigns. After alignment, the rms residuals in the positions of the IR counterparts to the radio sources are ~ 0.2 pixel, which corresponds to ~ 0.006 and ~ 0.01 in the 2.1 and 4.8 μm images, respectively.

Once the recalibrated images were updated with accurate WCS information, photometry was performed on Sgr A* and other stellar sources in the field using routines in the Astropy “*photutils*” software package. Circular apertures with a radius of 1.64 and 1.61 pixels with a pixel size of 0.03 were used for the 2.1 and 4.8 μm images, respectively, which is equivalent to aperture diameters of 0.10 and 0.20, respectively. Appropriate aperture corrections were applied to the measured fluxes based on the latest aperture correction data from STScI and converted to units of mJy.

2.2. Adjusting Timing Tags between 2.1 and 4.8 μm Data

An important part of our analysis of the Sgr A* light curves is the comparison in timing between flares in the 2.1 and 4.8 μm bands; hence, it is necessary to have accurate time stamps for each data point in the light curves. For all data, we use the midpoint of the integration from which the photometry is obtained. There is a discrepancy, however, in the effective midpoints of the 2.1 and 4.8 μm integrations. The 2.1 μm signal level in all pixels near Sgr A* is always low enough that detector saturation is never reached; hence, all groups from the “up-the-ramp” sampling for each integration are used to compute the flux. In the 4.8 μm data, however, signal levels are significantly higher and reach saturation sometime during each integration. The data reduction software automatically rejects the saturated groups when computing the signal for each integration, but this means that the effective time at which the data were obtained is shifted relative to the overall midpoint of the entire integration. We have determined at what point during the 4.8 μm integrations the data went into saturation and computed corresponding time-stamp corrections.

The data from days 1–3 are affected most severely by this issue, because longer integrations were used and hence a larger fraction of each integration was rejected due to saturation. For days 1–3, each integration had a length of 41.8 s, with the midpoint at 20.9 s. The 4.8 μm data saturated 12.6 s into each

integration, so the effective midpoint is at 6.3 s, 14.6 s earlier than the corresponding 2.1 μm data that used the full integration. Similarly, the shorter integrations used in day 4 resulted in the effective midpoint of the 4.8 μm data being 4.2 s earlier, and for days 5–7, the effective midpoint is 2.5 s earlier.

All subsequent analysis presented below has taken these timing offsets into account. In particular, for cases where the fluxes in the two bands are directly compared, the 4.8 μm data have been interpolated onto the same time grid as the 2.1 μm data.

2.3. Reference Stars and the Position of Sgr A* Aided by 230 GHz Observations

The NIR images shown in Figure 1 have used the astrometric registration technique described above (Section 2.1) to align them to the ALMA 230 GHz images. The actual coordinates for the aperture locations that we used for S0-17 and the reference “Ref” (Figure 1) in 2023 and 2024 are given in Table 2. The coordinates of these sources are derived relative to the ALMA image. The J2000 position of Sgr A* at epoch 2023.7 is derived from observations using ALMA obtained on 2023 August 25 and 2023 September 22 under project code 2022.A.00029.S using baselines up to 15 km. This position is within 10 mas (approximately one-third of the synthesized CLEAN beam) of the position predicted by the very long baseline interferometry proper-motion study of Sgr A* performed using the Very Long Baseline Array (D. Gordon 2023).

2.4. Background Subtraction

The aperture-based flux measurements of Sgr A* contain not only emission from Sgr A* itself but also diffuse background emission that is present throughout the images of the Galactic center, as well as contaminating flux from at least one nearby stellar source. The use of traditional background measurement techniques, such as the measurement of signal in an annulus around the Sgr A* aperture, does not result in an accurate estimate of the contaminating signal due to the highly nonuniform nature of the background components. We employed a combination of methods to estimate the total amount of extra signal in the Sgr A* aperture. This included an estimate of the diffuse background in the pixels immediately adjacent to the Sgr A* aperture in images taken when Sgr A* was at its lowest signal levels, as well as an estimate of the amount of contaminating flux from the immediately adjacent stars based on a model of its PSF and the amount of flux contained in the wings of that PSF that overlapped the Sgr A* aperture. This stellar contamination had to be estimated individually for each epoch of observations, due to the fact that the nearby stars are moving relative to Sgr A*. We used a constant background signal level for each day of data and subtracted it directly from the flux measured within the Sgr A* aperture. The final lists of corrected Sgr A* fluxes as a function of time were used to construct light curves for each day.

The actual measurements of “background” level arrived at doing photometry in background regions around Sgr A* were typically 0.16–0.19 mJy at 2.1 μm (across all 7 days) and 4.0–4.6 mJy at 4.8 μm . Note that at both wavelengths, the actual measurements increased by $\sim 15\%$ between the 2023 April and 2024 March–April observations due to movement of the nearby stars; thus, we picked up more flux from stars in the 2024 photometry using the same background region locations.

We attempted to estimate the amount of additional contamination contained in the Sgr A* aperture due to some members of the S cluster being adjacent to Sgr A* and spilling some of their fluxes into the Sgr A* aperture. We identified stellar sources in the S cluster by evolving their orbits to the epoch of our observations. The orbital parameters are taken from S. Gillessen et al. (2017). S0-2 is identified to be offset from Sgr A* by $0''.1745 \pm 0.0013$ and $0''.0006 \pm 0.0013$ to the north and east of Sgr A*, respectively, on 2023 August 22. Figure 1 (top right panel) shows the position of S0-2 with respect to Sgr A*. S0-2 was too far from Sgr A* and thus contributed little to no spilled flux in any epoch of these observations at 2.1 μm . However, two other members of the cluster, S24 and S29, which are relatively faint compared to S0-2, have approached closer (in projection) and hence spilled more flux in 2004 compared to 2003.

Similarly, at 4.8 μm , we estimated a total extra signal in the Sgr A* aperture of ~ 6.0 mJy in the 2023 data and ~ 6.3 mJy in the 2024 data. This is an increase over the actual measurements from the nearby background regions of ~ 2 mJy, with the extra 2 mJy being a ballpark estimate for the extra contamination due to nearby stars. So given the huge uncertainties in this process of estimating the extra contamination due to stellar contamination, possibly by S24 and S29, we have increased the 4.8 μm background flux by 1 mJy, thus accounting for possible oversubtraction at 4.8 μm .

2.5. Noise and Limits on Photometry

It is essentially impossible to empirically measure the random noise in the signal from Sgr A* because of its nearly constant variability in intrinsic flux level. Thus, the best proxies for estimating the noise limits of our photometry come from the data for S0-17, the additional reference star (“Ref”), and several randomly selected regions that have only faint, diffuse background emission. S0-17 and the background regions all have relatively low flux levels, comparable to or less than that of Sgr A*, and hence represent our ability to detect faint variations in Sgr A* emission. The measured noise levels at 2.1 μm are consistent across all seven epochs, while the data at 4.8 μm seem to be affected by our use of dithered (days 1–4) versus nondithered (days 5–7) observations. S0-17 and the background regions have an rms scatter of ~ 0.0015 mJy at 2.1 μm , suggesting a 3σ detection limit of ~ 0.005 mJy. At 4.8 μm , the rms scatter is ~ 0.03 – 0.04 for both S0-17 and the background regions but drops to ~ 0.01 mJy for the last three sets of nondithered observations, resulting in 3σ detection limits of ~ 0.1 and ~ 0.03 mJy for the dithered and nondithered data, respectively. When Sgr A* is in a flare state, we expect the total noise to be larger, due to increased Poisson noise. The reference star (“Ref”) has a 2.1 μm flux level comparable to the bright flare states of Sgr A* and 1σ noise of ~ 0.0035 mJy, which is a little more than twice the 1σ noise level of the fainter S0-17. Thus, we expect that the noise in the 2.1 μm fluxes from Sgr A* when it is in a flare state will also be higher by a similar amount, with a 3σ limit of ~ 0.01 mJy. We have not measured the 4.8 μm noise level in a reference star that is comparable in flux level to the flare states of Sgr A*, but we expect a similar increase relative to the noise in faint 4.8 μm sources and hence predict 4.8 μm 3σ noise levels of ~ 0.2 and ~ 0.07 mJy for the dithered and nondithered data, respectively.

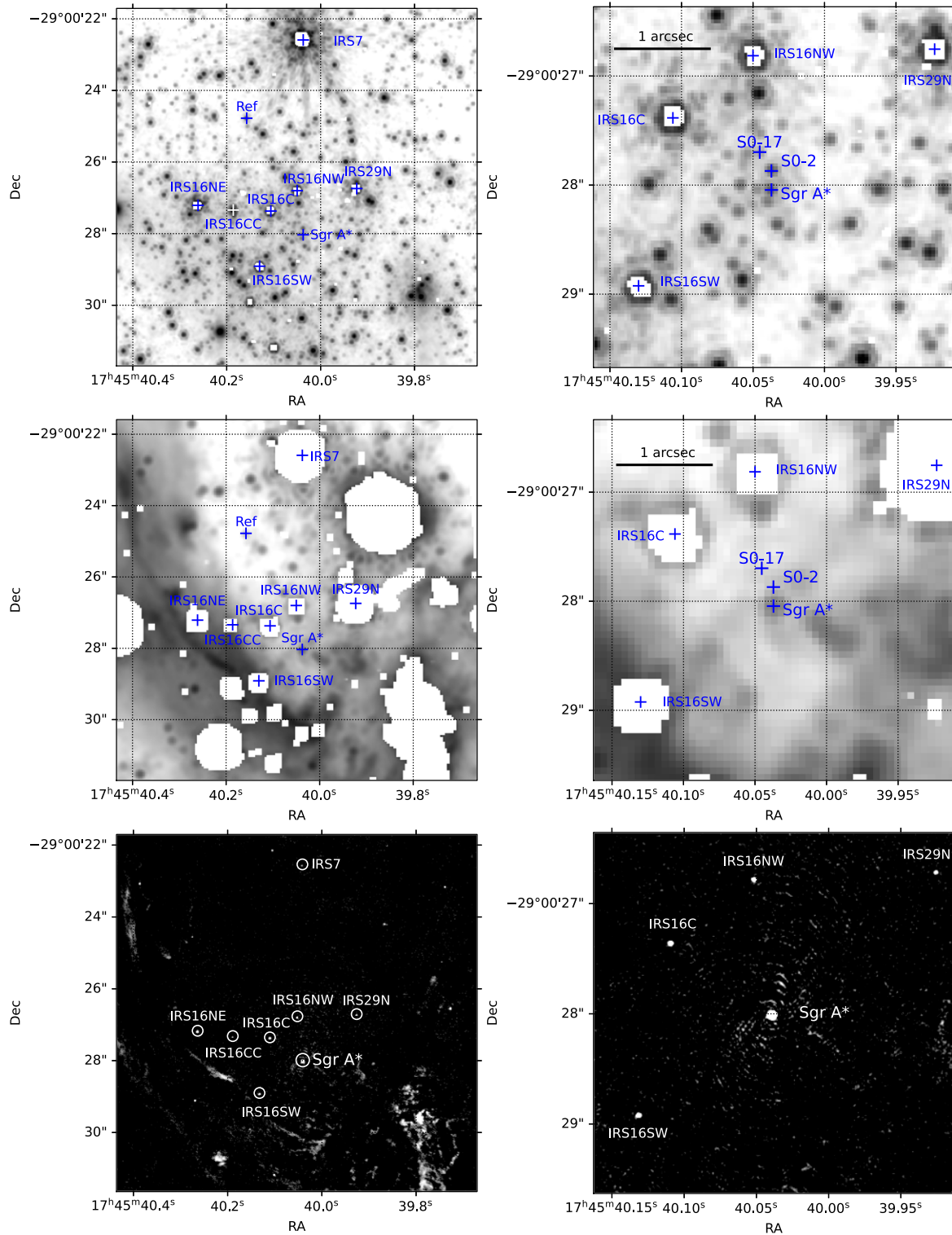


Figure 1. Astrometrically corrected NIRCam 2.1 μm (top) and 4.8 μm (middle) and ALMA 230 GHz (bottom) images of the Galactic center region. These images were simultaneously taken on 2023 September 22 and are astrometrically aligned with each other. Images on the left are zoomed out to show the locations of the well-known members of the stellar cluster, such as S0-2, orbiting Sgr A*, as well as the unidentified reference star (“Ref”) used to compare to Sgr A*. Images on the right are zoomed in to show the immediate vicinity of Sgr A* along with the comparison star S0-17. White pixels in the NIRCam images are completely saturated and have no usable signal values.

2.6. Extinction

Flux densities have been adjusted for extinction assuming $A_{K_s} = 2.46 \pm 0.03$ (for F210M) and $A_M = 1.0 \pm 0.3$ (for F480M; R. Schödel et al. 2011; S. D. von Fellenberg et al.

2024). We do not account for the differences between the K_s and F210M or between the M and F480M bands. The mean wavelengths only differ by $\lesssim 3\%$, which implies a $\lesssim 5\%$ change in the extinction, and different choices of extinction law can

Table 2
Coordinates of Sgr A* and Reference Stars

Name	Epoch	R.A. (J2000)	Decl. (J2000)
Sgr A*	2023 Aug–Sep	17 ^h 45 ^m 40 ^s .0323	−29° 00' 28."258
S0-17	2023 Apr–Sep	17 ^h 45 ^m 40 ^s .042	−29° 00' 27."95
S0-17	2024 Mar–Apr	17 ^h 45 ^m 40 ^s .042	−29° 00' 27."92
Reference star	2023 Apr–Sep	17 ^h 45 ^m 40 ^s .153	−29° 00' 25."02
Reference star	2024 Mar–Apr	17 ^h 45 ^m 40 ^s .154	−29° 00' 25."02

entail larger differences than this. Application of the adopted extinction correction increases the reported 2.1 and 4.8 μm flux densities by factors of 11.16 and 3.94, respectively. For the values reported here, the extinction correction is applied.

3. Results

We first concentrate on the analysis of Sgr A* variability, followed by the power spectrum analysis and the evolution of the spectral index variation as a function of time and flux density.

3.1. Light Curves

Short- and long-term variable emission from Sgr A* are presented followed by flux distribution of flaring activity. We considered a subjective way to classify the morphology of the light curves by flare, subflare, weak fluctuations, and pedestal emission, with the latter referring to slow variation of the intrinsic emission from Sgr A*. The pedestal level is distinct from constant background emission due to stellar light contamination that is subtracted from the flux of Sgr A*. Variations in the pedestal are fitted by a slope that varies from epoch to epoch.

We identify flares and subflares having extinction-corrected peak 2.1 μm flux densities ≥ 3 or $\lesssim 3$ mJy (corresponding to an observed flux density threshold of 0.27 mJy), respectively. Subflares generally have shorter durations, ≤ 20 minutes, either isolated or superimposed on rising and falling flares. The rationale for the choice of ~ 3 mJy becomes clearer when we discuss the flux and spectral index distributions indicating a transition from steep to shallow spectral index at a flux density of ~ 3 mJy. Finally, weak fluctuations in emission are identified at a level of $\lesssim 1$ mJy with short durations detected all the time.

3.1.1. Reference Star Light Curves

Figure 2 shows a comparison of linear- and logarithm-scale light curves of the reference star S0-17 and reference stars at 2.1 and 4.8 μm and those of Sgr A* on all 7 days. The gaps between different epochs are not displayed in order to show the nature of long-term variability of Sgr A* on daily, monthly, and yearly timescales. S0-17 acts as a common reference star in all epochs of data. The light curves of S0-17 indicate that the fluxes are very stable and flat with a flux density (uncorrected for extinction) of 0.409 ± 0.001 mJy and 4.44 ± 0.02 mJy at 2.1 and 4.8 μm , respectively.

The flatness and stability of the reference starlight curves provide strong support on the continuous low-level weak and strong variable activity of Sgr A* at both wavelengths on all 7 days. Due to the proximity of S0-17 and Sgr A*, the measured light curve of S0-17 is slightly contaminated by Sgr A* flare emission, especially at 4.8 μm , where the PSF of Sgr A* is more extended.

3.1.2. Short-term Flux Variability

Figure 3 shows extinction-corrected light curves of the seven epochs of observations in 2023 and 2024. There is clearly correlated variability at 2.1 and 4.8 μm in all epochs. Day 2 showed the strongest flare emission in the 2023 epochs at ≥ 6 mJy at 2.1 μm . However, the peak of this flare was missed due to poor guiding of the telescope. Only 2.1 μm data are available on day 3 due to Sgr A* being outside the 4.8 μm field of view, which was caused by an error in guide star acquisition. Three flares, each lasting for a total duration of about 1 hr, are detected. A number of subflares and weak fluctuations are superimposed on the three flares. Similarly, day 4 observations suffered from intermittent poor guiding and were terminated early due to a complete loss of the lock on the guide star. We note two flares, each lasting for more than 1 hr, with a number of superimposed subflares.

In the 2024 observations (days 5–7), no dithering was done, allowing us to obtain continuous light curves with a short sampling time and no gaps. Days 5 and 6 each showed three flares, and day 7 showed two flares. We also note the long flare duration (≥ 30 minutes), multiple subflares, and continuous weak fluctuations with short durations superimposed on flares in 2024. In particular, six subflares noted that the strongest intensity, ~ 30 mJy at 4.8 μm , has the longest duration between ~ 11 hr and ~ 12.50 hr UT on day 7.

One striking result is the nonstop intensity fluctuations of the variable emission from minute to hourly timescales, probing event-horizon-size scales, which will be discussed in Section 3.2. Correlated variability between 2.1 and 4.8 μm emission is detected throughout all seven epochs of observations. The light curves suggest that the subflares and low-level fluctuations are superimposed on the strong flaring component with longer duration. A trend that we note in multiple flares is that subflares become increasingly stronger on the rising and/or falling sides of flaring events. Some examples that are found are subflares near 8.75 UT on day 1, 10.50 UT on day 3, 6.75 UT on day 4, 8.50 on day 5, 10.50 UT on day 6, and 11.75 UT on day 7. The frequency of an asymmetry in the rise and fall of flares is most noticeable when subflares are detected on the rising side. The best example is on day 5, where the flare starts rising near 8.0 UT with three subflares followed by a peak near 9.00 UT before the flare finally falls steeply. If the subflares and flares are physically associated with each other, then one could consider that subflares are precursors of bright flares. There are also events in which subflares are noted on the falling side of bright flares. The best example is on day 6 near 10.25 hr UT, where the flare initially rises rapidly to a peak of ~ 24 mJy at 4.8 μm before falling with multiple subflares near 10.75 hr UT. We cannot quantify this morphological aspect of flaring events.

3.1.3. Long-term Flux Variability

The seven panels of Figure 3 show that the pedestal level at which short-term variability is detected is different on all days of observations. In addition, there is evidence that the pedestal flux level evolves as a function of time and shows a slope. The solid lines are fourth-degree polynomial fits to the data with the added constraint that the polynomials never exceed the data. Appendix A gives details of the chosen fits. These polynomials are thus one way to estimate the slow variation of the pedestal emission of Sgr A* that underlies the flares. The differing curves

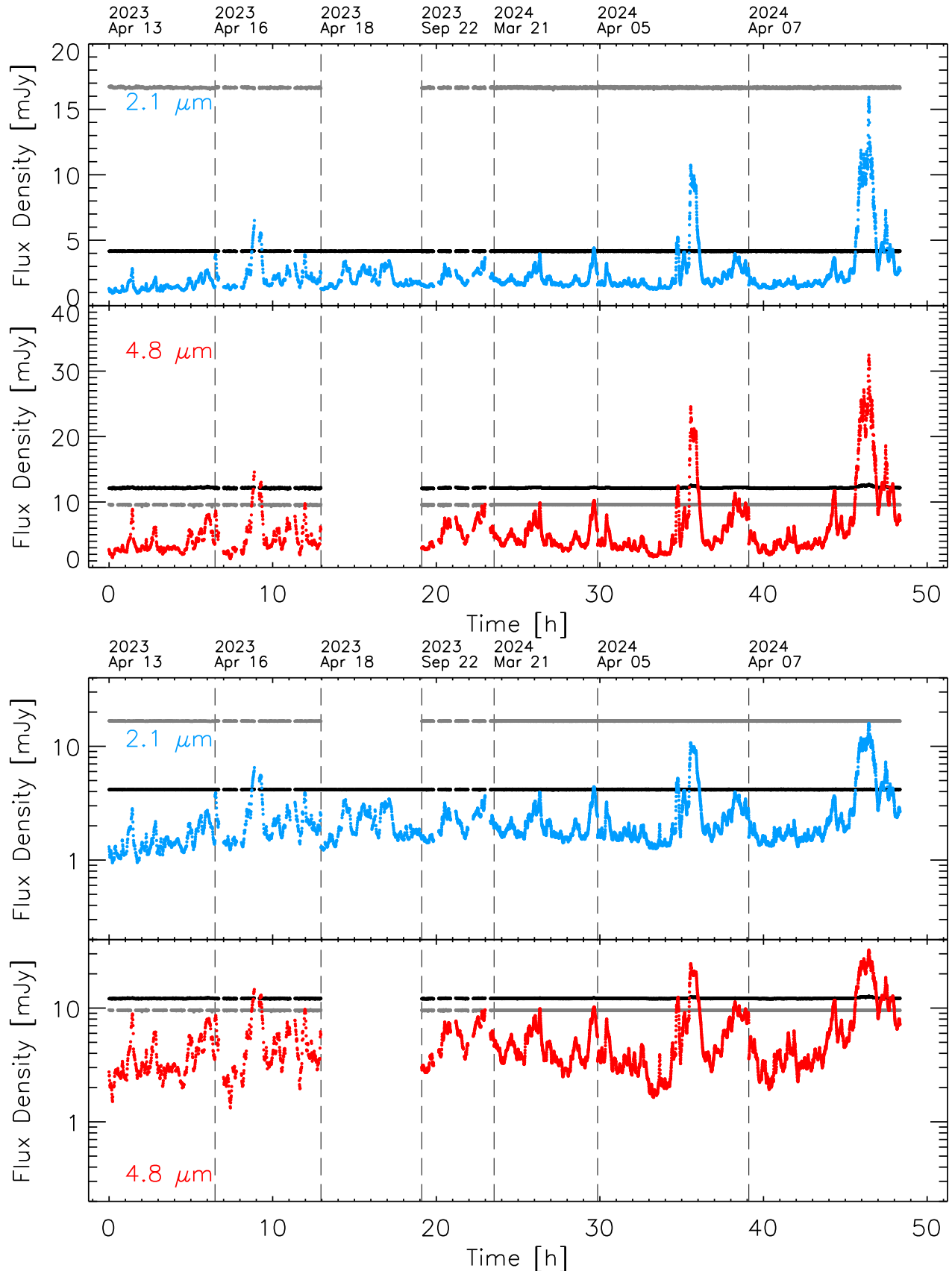


Figure 2. Extinction-corrected light curves of Sgr A* and reference stars for all 7 days concatenated together at 2.1 and 4.8 μm are presented in linear and logarithmic scales in the top and bottom panels, respectively. The light curves of the reference stars S0-17 and “Ref.”, a random nearby star in the field with a similar signal level as Sgr A*, are displayed in the top panel as black and gray points, respectively. The reference stars are stable, whereas Sgr A* is always fluctuating. Vertical dashed lines separate 7 different noncontiguous days. These plots indicate that the observed variations in Sgr A* at both wavelengths are real and not an artifact or noise. In addition, the amplitude of the quiescent flux of Sgr A* and pedestal emission vary on daily, monthly, and yearly timescales.

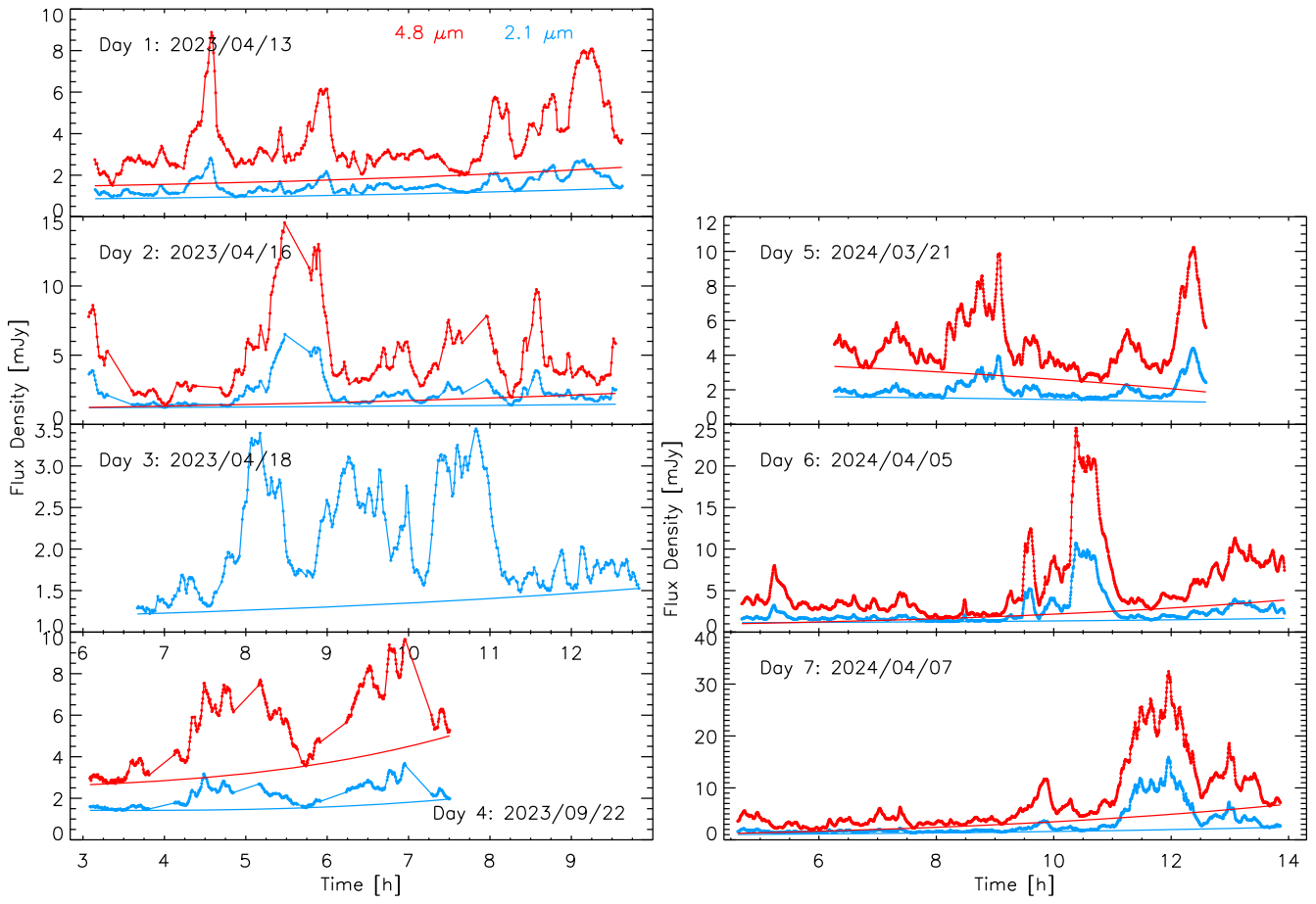


Figure 3. Left: four panels show light curves of Sgr A* by connecting the data points and are constructed, days 1–4, of observations in 2023. Blue and red dots correspond to 2.1 and 4.8 μm , respectively. The sampling time is 46 and 25 s on days 1–3 and day 4, respectively (see Table 1). Correlated variability is detected. Extinction corrections have been applied. The extinction correction increases the measured 2.1 and 4.8 μm flux densities by factors of 11.16 and 3.94, respectively. Linear fits to the changing pedestal have been made in all epochs at 2.1 (blue) and 4.8 (red) μm . To estimate the pedestal, the solid lines are fourth-degree polynomial fits to the data. The differing curves indicate that the pedestal varies in brightness and spectral index. There is a tendency to be relatively redder when flaring is brighter, but this could be an artifact of the estimated background level that has been subtracted from all Sgr A* photometry. Note that the F480M filter was not available on day 3. These figures show the evidence for long-term variability of the quiescent emission (pedestal) from Sgr A*. Right: similar to the left panels except that the light curves of days 5–7 in 2024 are displayed. The sampling time is 18.2 s in days 5–7 in 2024. Correlated variability in both the F210M and F480M bands is detected. The 1σ error bars at 2.1 and 4.8 μm are 0.0015 and 0.03 mJy, respectively, and are too small to display.

at the two wavelengths on each day indicate that the pedestal varies in color or spectral index as well as brightness. The background can be blue or red in terms of spectral index. There is a tendency to be relatively redder when flaring is brighter, but this could be an artifact of the chosen photometry backgrounds. The light curves also show pedestals with amplitudes that vary between each epoch, suggesting that there is long-term variability of Sgr A* on daily, monthly, and yearly timescales. The pedestal is varying roughly by a factor of 2 over seven epochs of observations. These trends are best illustrated in Figure 2, where all data are plotted on a single constant scale. Examples that show that Sgr A* pedestal emission is not constant can clearly be viewed in the fits of all days. A representation of this trend can be found in the top and bottom panels of Figure 3, where logarithm- and linear-scale light curves of all seven epochs show nonstop variability of Sgr A*. In the concatenated light curves in the top panel, it seems more clearly evident that the 2.1 μm pedestal emission on day 1 is lower and on day 7 is higher than on days 2–6. These suggest day-to-day, month-to-month variations in the background intrinsic to Sgr A*.

Another trend that we note is the apparent correlation of strong flares with the pedestal emission. We note that this trend

is detected on multiple days where there are strong flaring events. For example, strong flaring activity between 9 and 14 hr UT on day 6 shows a stronger pedestal at the end of the activity (right panel of Figure 3). In fact, in almost all days, we detect an increase in the pedestal flux when there are groups of strong flares. It is difficult to quantify this correlation, given the frequency of flaring events. Nevertheless, this trend implies that strong flare emission arising from localized hot spots is correlated with the global structure of the accretion flow, represented by varying pedestal flux.

3.1.4. Flux Density Gradient of the Variable Emission

Another feature that we notice in the light curves of Sgr A* is the sudden rise or drop in the flux density over a short time interval. For all seven epochs, we determined the flux-normalized derivative of the flux density as a function of time between any two adjacent data points normalized by the flux density. The two panels of Figure 4 show the intensity gradients of day 6, where the highest values are seen. The mean gradients for all days roughly range between $\sim 5\text{ hr}^{-1}$ during low-level intensity fluctuations and $\sim 10\text{--}20\text{ hr}^{-1}$ for typical subflares. The highest values are noted near strong flares on day

Table 3
LN and Power-law (PL) Fit Parameters for Flux Density Histograms

Wavelength (μm)	Model Fits	χ^2	Peak	μ_{\ln}	σ_{\ln}	β	x_{\min}
2.1	LN	163.16	460.26	0.64	0.21		
2.1	LN+PL	61.48	504.76	0.64	0.19	-3.99	1.847
2.1	2LN	133.100	460.26	0.64	0.19		
2.1			11.37	2.30	0.065		
4.8	LN	113.35	1101.62	1.49	0.35		
4.8	LN+PL	85.77	998.45	1.33	0.244	-2.96	4.02
4.8	2LN	82.11	1097.98	1.48	0.35		
4.8			33.44	3.11	0.08		

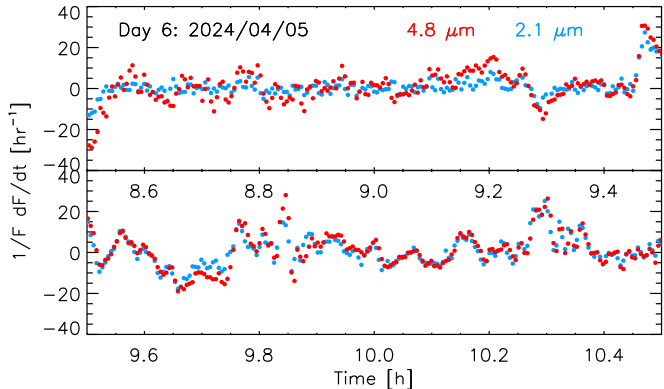


Figure 4. Values of the time derivative of day 6 data normalized by the flux density as a function of time are presented in the top and bottom panels. Three examples in which values are highest are near 9.5, 9.85, and 10.3 UT, showing a change in the flux density by a factor of e in $\sim 2\text{--}3$ minutes.

6 near 9.5, 9.85, and 10.3 UT with a gradient $\sim 30 \text{ hr}^{-1}$, which corresponds to a factor of 2 in flux variation in 1.39 minutes. This timescale is not limited by the ~ 18 s sampling time measured on day 6. This short timescale places a constraint on the particle acceleration mechanism at work during an infrared flare at NIR wavelengths.

3.1.5. Flux Distribution of the Variable Emission

As shown in Figures 2–4, Sgr A* shows a wide range of flux density values over seven epochs of observations. The mean, median, and 1σ error flux densities for each day are tabulated in Table 3. The median flux densities at 2.1 and 4.8 μm are in the ranges 1.39–2.03 and 2.05–4.70 mJy, respectively. The median flux density of the GRAVITY measurements (GRAVITY Collaboration et al. 2020) is 1.1 ± 0.3 mJy at 2.1 μm . The discrepancy is most likely due to flux variability measured in different epochs.

Figure 5 shows the histogram of the flux distribution for all seven epochs of data at 2.1 and 4.8 μm . All light curves were resampled at 2 minute intervals for these histograms in order to avoid overrepresenting day 5–7 observations, which employed higher sampling rates than the earlier days (see Table 1). The histogram suggests two populations of faint and bright emission with two peaks near 2 and 10 mJy at 2.1 μm . The bottom panel shows the cumulative fraction of time that the flux is below a certain value. In particular, we note that there is a shoulder between the fainter (subflare) emission and brighter (flare) emission at ~ 3 and ~ 9 mJy at 2.1 and 4.8 μm , respectively.

The cumulative fraction of time of the variability of Sgr A* indicates that flare emissions with flux densities greater than ~ 3 and ~ 9 mJy at 2.1 and 4.8 μm are at a level of 10% where bright flares occur. The remaining $\sim 90\%$ are detected at flux densities with a range between 1 and 3 mJy at 2.1 μm and 1.6 and 9 mJy at 4.8 μm . These limits suggest two different populations having different spectral indices.

Following K. Dodds-Eden et al. (2009), we model the flux density histograms with lognormal (LN; light green) and tailed LN (dark green) distributions and the sum of two LN distributions, as shown in Figure 5. The parameters of the fits are listed in Table 3, including χ^2 , the amplitude of the peak, the natural log of the mean flux density (μ_{\ln}), the widths (σ_{\ln}), the power-law index (β), and the lower-limit cutoff (x_{\min}) values of three different distributions.

The tailed LN distributions in Figure 5 represent the data better than the simple LN distribution at 2.1 μm . At 2.1 μm , the mean (μ_{\ln}) of the LN distribution corresponds to ~ 1.90 mJy. The two-LN distribution is a better fit at 4.8 μm but not at 2.1 μm . In this case, the mean flux densities for the two-LN distributions are 3.22 and 21.32 mJy. The result shows the presence of a bright component that is distinct from the fainter component, but with relatively little data at the brightest levels, it is impossible to precisely characterize the functional distribution of the bright emission. However, the 4.8 μm data suggest two states described by two-LN distributions for faint and bright variability of Sgr A*, as found by K. Dodds-Eden et al. (2009).

3.2. Power Spectrum of the Flux Variability

The power spectra of the light curves for each day are shown in Figure 6. The dominant feature is a power-law slope. There is no indication of any strongly periodic behavior at any frequency. Most spectra do show flattening at high frequencies, which is consistent with reaching the effective noise level of the observations. Most spectra also show flattening at the lowest frequencies, which is an intrinsic feature of the light curves. The frequency turnover noted at low frequencies is indicative of suppression of low-frequency power that might have been expected (e.g., high pass filtering). However, the turnover frequency from red spectrum to white spectrum changes in every epoch.

To quantify these trends, we fit each power spectrum with the sum of a broken power law and a white-noise component,

$$P(f) = P_0 \quad f < f_0 \quad (1)$$

$$= (P_0 - P_1)(f/f_0)^n + P_1 \quad f \geq f_0, \quad (2)$$

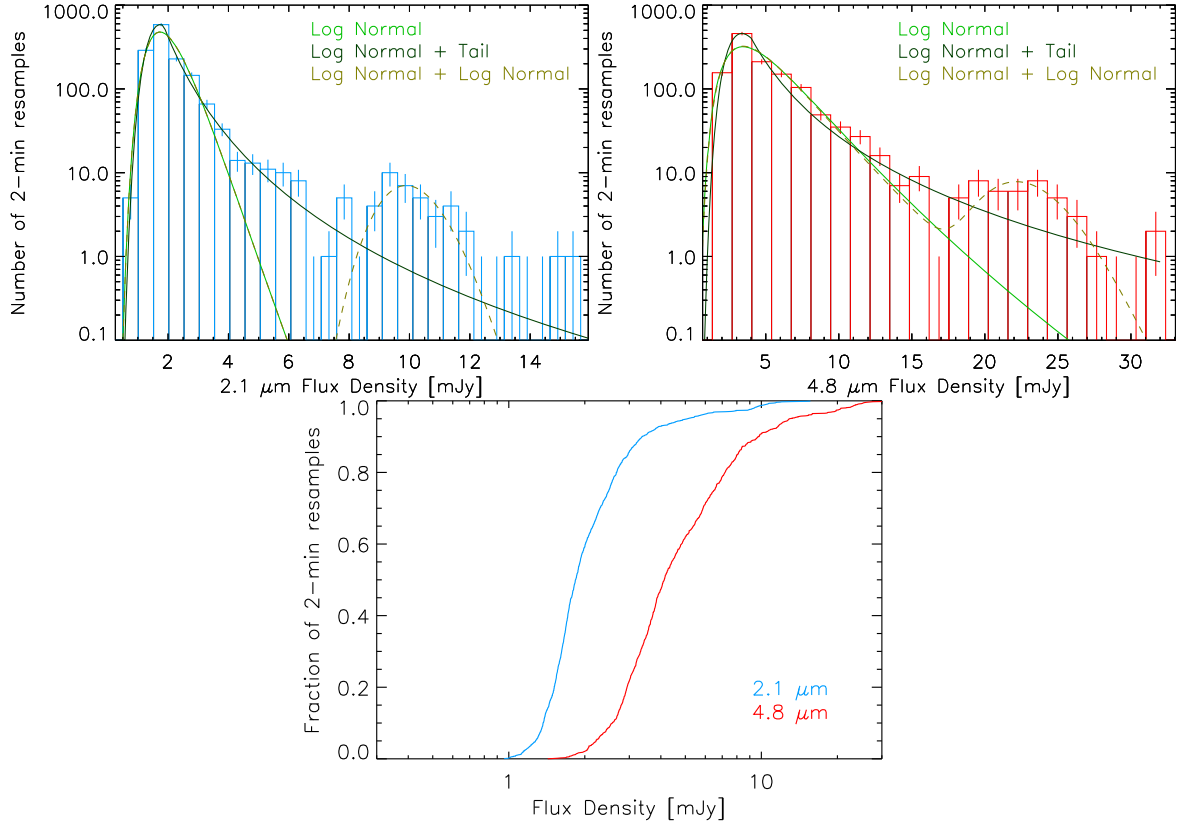


Figure 5. Using all seven epochs of observations, histograms of the flux distribution of Sgr A* at 2.1 and 4.8 μm are displayed in the top left and right panels, respectively. LN (light green line), LN-plus-power-law (dark green line), and two-LN (dashed green line) distribution fits to the histograms are shown. The two-LN and LN-plus-power-law fits are reasonable representations of weak fluctuations at 4.8 and 2.1 μm , respectively. Other distributions give failed solutions to fit strong fluxes (see Table 3 and text). The histograms indicate two populations of the variable emission. The $1\sigma = \sqrt{N}$ error bars are shown on the histogram bins. The bottom panel shows the fraction of time at which Sgr A* is observed below a given flux density.

Table 4

Mean, Median, and Sigma Fluxes (mJy) for Each Day

Epoch	Median 2.1 μm	Mean 2.1 μm	Sigma 2.1 μm	Median 4.8 μm	Mean 4.8 μm	Sigma 4.8 μm
Day 1	1.39	1.52	0.41	3.05	3.69	1.53
Day 2	2.03	2.28	0.99	3.97	4.80	2.57
Day 3	1.84	2.07	0.60	0.00	0.00	0.00
Day 4	2.15	2.15	0.52	5.70	5.49	1.82
Day 5	1.86	2.04	0.58	4.25	4.69	1.65
Day 6	1.83	2.47	1.72	3.95	5.60	4.25
Day 7	1.92	3.21	2.82	4.90	7.77	6.49

where P_0 is the power at the break frequency, f_0 , between the (assumed) flat spectrum and the power law; n is the power-law index; and P_1 is the white-noise power level. An additional derived parameter, $f_{1/2}$, gives the frequency where the power-law and white-noise components contribute equally to the total power,

$$f_{1/2} = f_0 [P_1/(P_0 - P_1)]^{1/n}. \quad (3)$$

These parameters are listed in Table 5. The quoted uncertainties are the standard deviations of 1000 Monte Carlo realizations of power spectra calculated from data with random noise added (1σ is the added random noise from the photometric uncertainties). We note a strong anticorrelation between the derived n and f_0 parameters on each day; thus, higher break

frequencies (shorter periods) are noted for steeper power spectrum indices.

Unsurprisingly, the parameter P_0 largely tracks the overall brightness of the flaring events on different days. The break frequency, f_0 , does appear to vary from day to day, but its value is poorly constrained because it is relatively close to the lowest frequency of the observations. Across the 7 days, the power-law indices have mean values of $n = -3.0 \pm 0.3$ at 2.1 μm and $n = -3.0 \pm 0.4$ at 4.8 μm . Shallower power-law indices are generally found on days when the flattening at high and/or low frequencies is not as clearly distinguished. There are strong covariances between the parameters of these fits, so flatter power laws would be expected if f_0 and or P_1 are underestimated.

Table 5 shows the power spectrum break at low frequency with 1σ error on each day at 2.1 and 4.8 μm . The existence of this break that varies from epoch to epoch suggests a physical mechanism that ties the low-frequency variability to higher frequencies that follow a power-law spectrum. Longer-duration observations of Sgr A* are required to confirm the break in the power spectrum at low frequencies. There is variation from the day-to-day timescale, and the timescales of the break are much shorter than the 8 hr timescale estimated from submillimeter data (J. Dexter et al. 2014).

The physical mechanism that produces the power law is altered or limited on longer timescales. If the timescales correspond to light travel times, then this would also suggest that the processes causing the variability act coherently on scales $\gtrsim 100$ light-minutes. Uncorrelated white noise has also

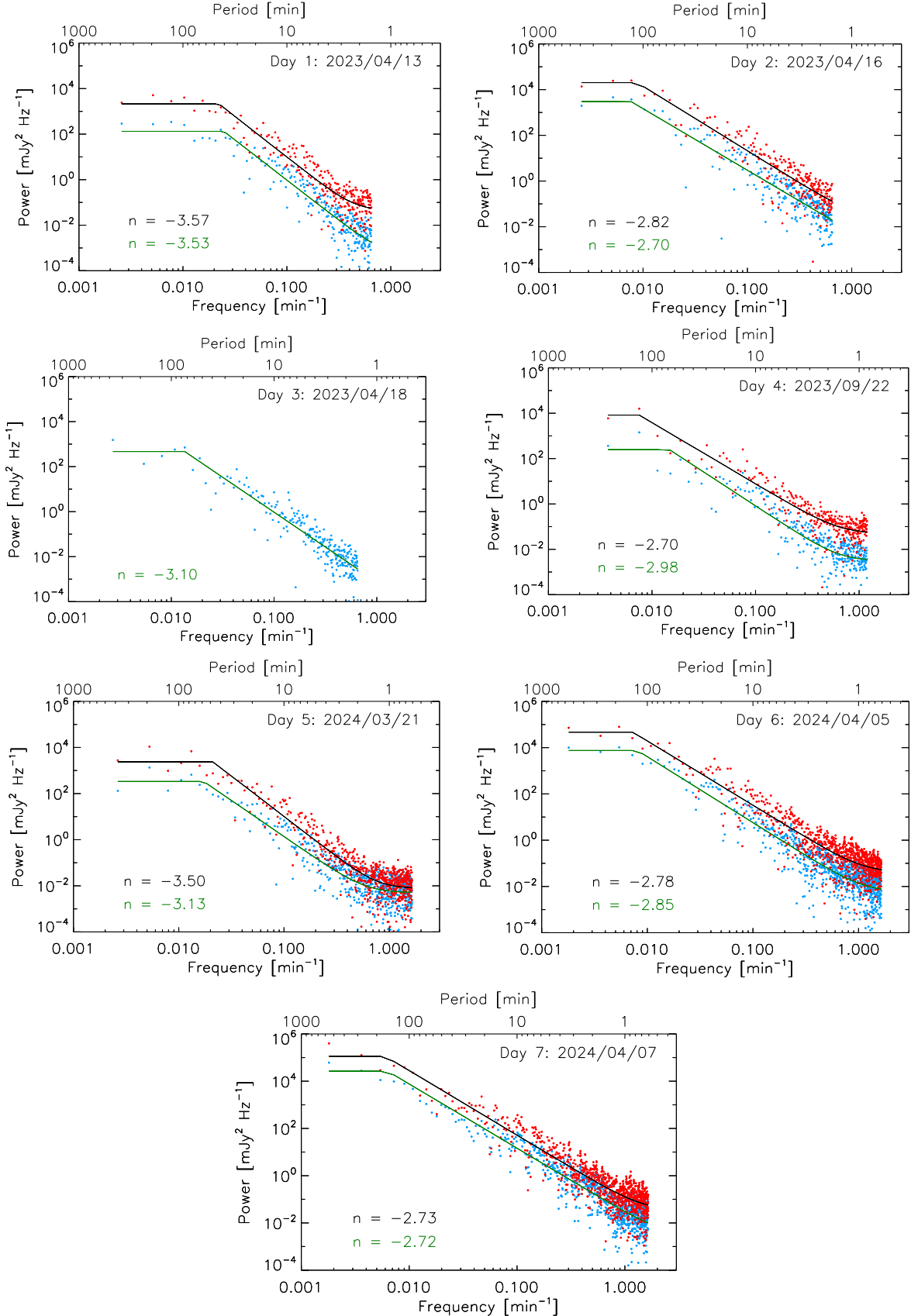


Figure 6. Power spectra of the temporal variations of Sgr A* on a log-frequency scale in the F210M (blue) and F480M (red) bands are presented for each epoch of observation. The data for each epoch are fitted with broken power-law trends over the frequency ranges indicated by the solid lines with a transition frequency where the power-law distribution becomes flat at low f_0 and high frequencies $f_{1/2}$ (see Table 5). The power-law index n is indicated in the figure. These plots show evidence of Sgr A*'s variability, displaying two different statistics on short- and long-term timescales at frequencies $f \geq f_0$ and $f < f_0$, respectively. Note that the transition frequency f_0 changes in every epoch, supporting long-term quiescent variability of Sgr A*, though longer continuous observations are needed to confirm this result.

Table 5
Power Spectrum Parameters

Day	Wavelength (μm)	P_0 ($\text{mJy}^2 \text{Hz}^{-1}$)	n	f_0 (minute $^{-1}$)	P_1 ($\text{mJy}^2 \text{Hz}^{-1}$)	$f_{1/2}$ (minute $^{-1}$)
2023 Apr 13	2.1	132.4 ± 2.5	-3.53 ± 0.11	0.0247 ± 0.0015	0.000 ± 0.002	0.8567
2023 Apr 13	4.8	2127.2 ± 25.3	-3.57 ± 0.12	0.0222 ± 0.0016	0.044 ± 0.026	0.4556
2023 Apr 16	2.1	3008.4 ± 9.4	-2.70 ± 0.04	0.0077 ± 0.0003	0.000 ± 0.005	Infinity
2023 Apr 16	4.8	$20,331.7 \pm 68.6$	-2.82 ± 0.07	0.0088 ± 0.0004	0.023 ± 0.058	1.1305
2023 Apr 18	2.1	468.8 ± 2.7	-3.10 ± 0.07	0.0135 ± 0.0005	0.000 ± 0.002	Infinity
2023 Apr 18	4.8
2023 Sep 22	2.1	248.8 ± 12.1	-2.98 ± 0.08	0.0147 ± 0.0003	0.003 ± 0.002	0.6536
2023 Sep 22	4.8	8277.3 ± 597.2	-2.70 ± 0.06	0.0075 ± 0.0000	0.048 ± 0.016	0.6560
2024 Mar 21	2.1	336.0 ± 2.0	-3.13 ± 0.08	0.0172 ± 0.0008	0.005 ± 0.001	0.6007
2024 Mar 21	4.8	2377.6 ± 11.2	-3.50 ± 0.07	0.021 ± 0.0006	0.008 ± 0.004	0.7792
2024 Apr 5	2.1	7527.6 ± 10.3	-2.85 ± 0.05	0.0081 ± 0.0006	0.006 ± 0.002	1.1222
2024 Apr 5	4.8	$46,598.2 \pm 87.3$	-2.78 ± 0.04	0.0073 ± 0.0006	0.040 ± 0.008	1.1146
2024 Apr 7	2.1	$26,604.8 \pm 26.6$	-2.72 ± 0.03	0.0063 ± 0.0002	0.003 ± 0.002	2.3447
2024 Apr 7	4.8	$113,080.7 \pm 142.7$	-2.73 ± 0.03	0.0060 ± 0.0002	0.033 ± 0.009	1.4829

been reported at timescales greater than $\sim 270_{-94}^{+261}$ minutes (G. Witzel et al. 2018) and $\sim 128_{-77}^{+329}$ (L. Meyer et al. 2009).

3.3. The Spectral Index versus the Flux Density

Given the unique capability of NIRCam to observe two NIR wavelengths simultaneously, the spectral index α of bright and faint flares can be determined as a function of time. The top left panel of Figure 7 shows the variation of 4.8 μm against 2.1 μm flux density for all 7 days. A correspondingly colored version of the light curves for all data is shown in the top right panel Figure 7. The colors denote 6 days of observations at 2.1 and 4.8 μm , as indicated in the light curves. The strongest flaring activity displayed in red on day 7 tends to show a shallower slope. A striking result is the anticorrelation and correlation reflecting a variation of the slope that becomes shallower as the flux density increases. This is consistent with two different populations of energetic particles producing faint and bright variable emission. The variation of the spectral index as a function of F210M flux density is displayed in the middle left panel. The mean spectral index tends to become steeper with increasing brightness up to ~ 3 mJy at 2.1 μm without any further steepening at higher brightnesses. The weak anticorrelation of the spectral index with brightness (up to a limit) changes and shows a shallower spectral index with increasing brightness. The spectral index eventually saturates with increasing brightness with values close to $\alpha \sim -1$. The middle right panel of Figure 7 shows the spectral index variation as a function of time for all epochs. The four panels of all data presented in Figure 7 are shown for individual days in Appendix B, Figures 10–15.

One of the most challenging aspects of this unusual behavior of the positive spectral index is the background emission due to contamination by stars in the vicinity of Sgr A*. In order to investigate the effect of varying the estimated background emission, scatter plots of the 2.1 and 4.8 μm flux densities for all days are shown in the upper left panel of Figure 7. Overlaid on this figure are lines indicating the loci of constant spectral index. The lines in color are linear fits to the photometry on each day, which will be discussed in Section 3.3.1. We note that the fainter data points have $\alpha \sim -1.58$ and the spectral index becomes shallower to $\alpha \sim -0.85$ for the brighter data points.

We also examined the impact of changing the background flux level at 4.8 μm of day 7 data only (red color in the middle left panel of Figure 7), as shown in the bottom panel of Figure 7. It is clear that the overall trend remains unchanged, but the positive spectral index of the weak flux densities disappears when the background emission increases by 1 and 2 mJy, which has the effect of increasing the brightness of Sgr A*. There is clearly an uncertainty in the spectral index of the weakest emitting fluctuations. However, the key point is that in spite of this uncertainty in the 4.8 μm background flux density by 1 or 2 mJy, the slopes in the flux versus flux plots are independent of the background level. The slopes are independent of the background level, thus supporting the bimodality of flare emission from Sgr A*. How those slopes translate into spectral indices depends on the choice of background level.

3.3.1. Linear Fits to the Slope of 2.1 versus 4.8 μm Flux Density

We have fitted broken linear fits to the flux density of 4.8 μm versus 2.1 μm for all days, as shown in Figure 7 (top left panel). Fits to the flux density for individual days are shown in Figures 10–15 in Appendix B. The fits are given by the following equation:

$$S(4.8) = S_0(4.8) + a_{\pm} \times (S(2.1) - S_0(2.1)), \quad (4)$$

where $S(2.1)$ and $S(4.8)$ are flux densities at 2.1 and 4.8 μm , respectively; S_0 is the flux density where the slope changes; a_+ applies for $S(2.1) \geq S_0(2.1)$; and a_- applies for $S(2.1) \leq S_0(2.1)$. These fits use four parameters, as given in Table 6. The values α_- and α_+ are the slopes, a , translated into constant power-law indices. The mean spectral indices over all days are -1.58 ± 0.150 and -0.87 ± 0.16 for the faint and strong variable emission, as listed in the last column. The values would change if the offsets in either band were changed, so their values could differ. The a_{\pm} values are important in that they are independent of whatever offset or background adjustment is made.

The fact that the slope values for all days and individual days, as displayed in Appendix B, seem to cluster around the “all days” values of 3.7 and 2.0 suggests a consistent picture that there are two populations of flares with a spectral index that changes from steep to shallow as the flares become brighter. The dependence of the spectral index on the flux

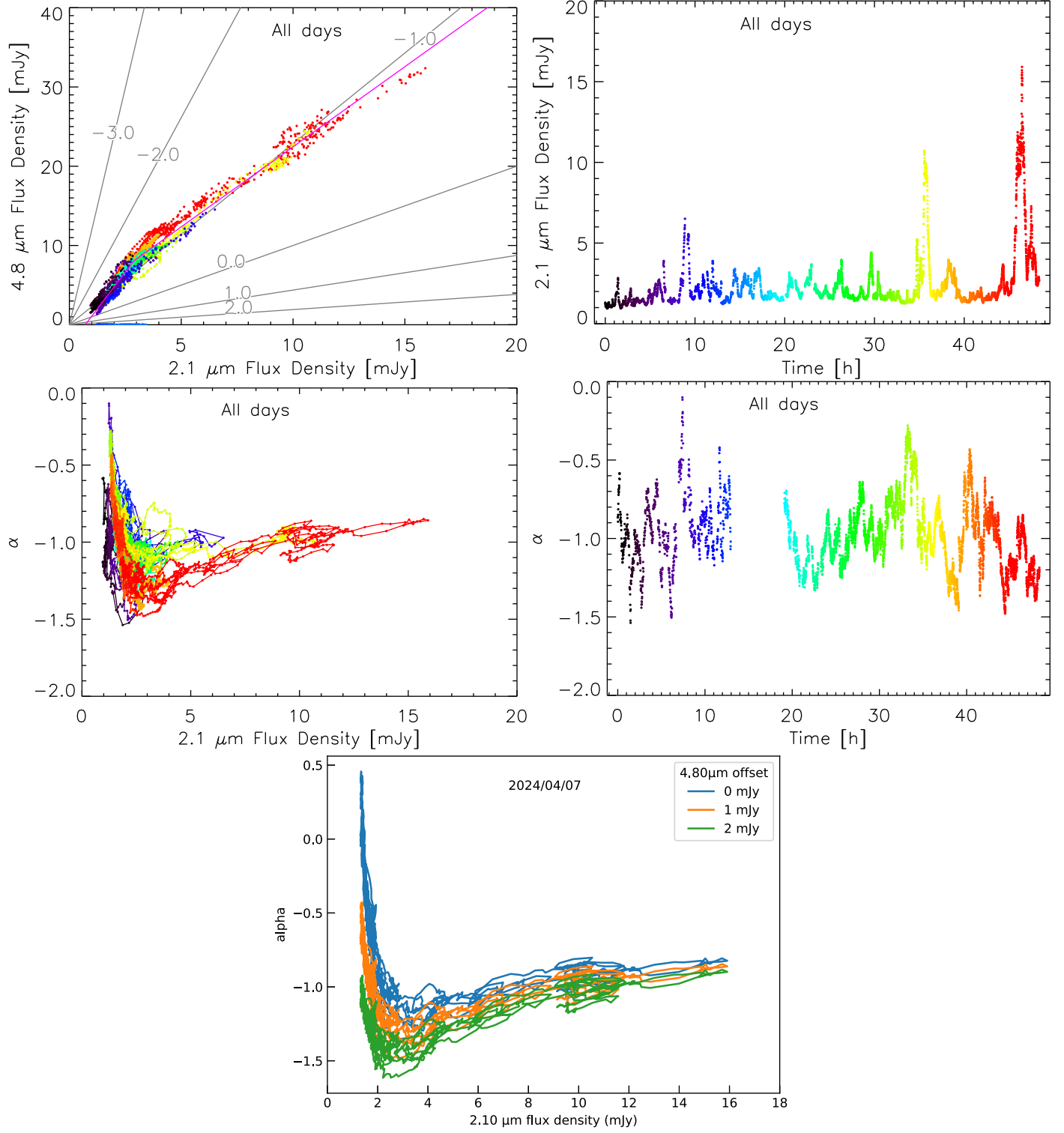


Figure 7. Top left: a scatter plot of the F210M and F480M flux densities on all days overlaid with loci of constant spectral index. The magenta line is a broken linear fit to the data, with parameters listed in Table 6. The slope for the fainter data points corresponds to a spectral index $\alpha \sim -1.58$, whereas the slope for the brighter data points, the spectral index flattens to $\alpha \sim -0.85$. The change in the slope suggests two different populations with different spectral indices. Top right: light curves of Sgr A* at 2.1 μm for all epochs. Middle left: the spectral index of Sgr A* as a function 2.1 μm flux density for all six epochs of observations. Middle right: the spectral index evolution for all six epochs. The colors correspond to the times indicated for each epoch. Bottom: the spectral index vs. 2.1 μm flux density on day 7 if the 4.8 μm subtracted background is reduced by 1 and 2 mJy. Given that the background 4.8 μm flux is more likely to be contaminated by nearby stars than the 2.2 μm flux of Sgr A*, the positive spectral index of faint variable emission (shown in blue) disappears when the 4.8 μm flux is increased by 1 mJy. However, the bright flare's spectral indices and the trend are not affected by the background change.

density resembles another characteristic that distinguishes weak and bright flares, namely, different statistics applied to the flux distribution of faint and bright flares, as described in

Section 3.1.4. 2.1 μm \sim 3 mJy seen here is another reason for the distinction between flares and subflares as defined previously.

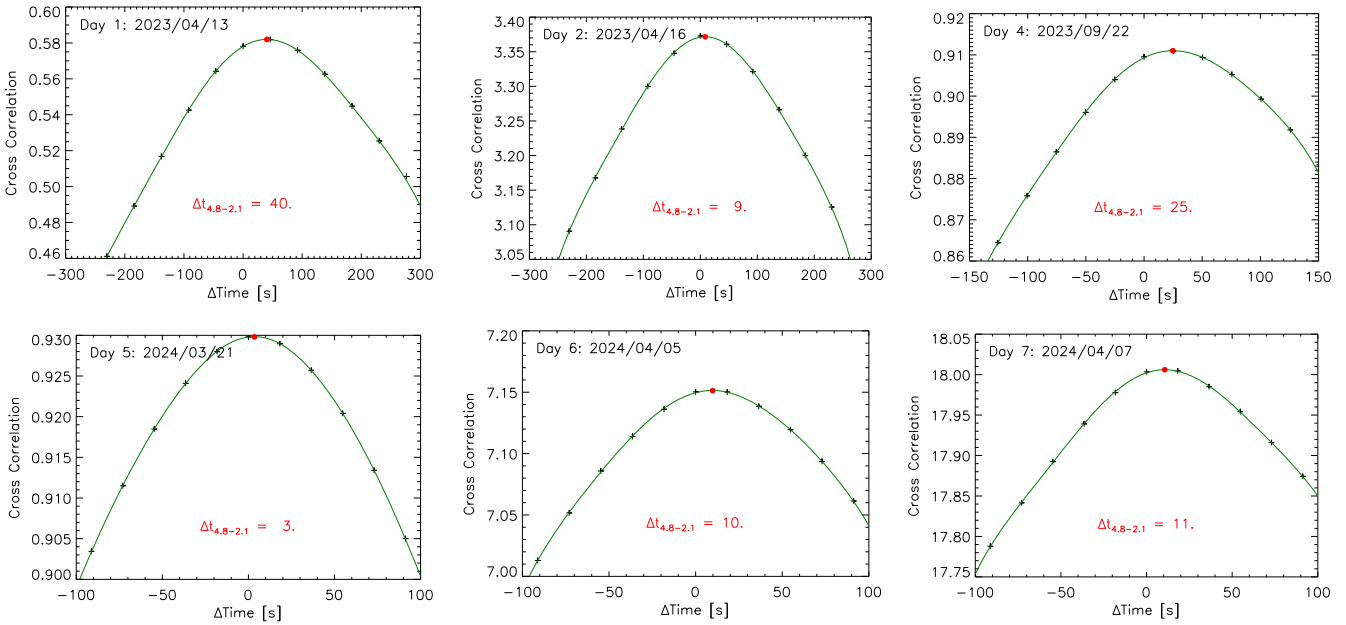


Figure 8. Cross-correlation of the Sgr A* light curves in the F210M and F480M bands as a function of time are shown for each of the six epochs of observations. Epochs 1, 2, and 4 are displayed in the top three panels, whereas epochs 5, 6, and 7 are displayed in the bottom panels. The cross-correlations indicate time delays in the range between 3 and 40 s. Positive Δt , as shown in red in each figure, corresponds to F210M variations preceding those at F480M.

Table 6
Parameters of Linear Fits to 2.1 μm vs. 4.8 μm Flux Density

Date	S_0 (2.1 μm)	S_0 (4.8 μm)	a_-	a_+	α_-	α_+
All	2.90	8.10	3.70	2.02	-1.58	-0.85
Day 1	3.33	...	-1.46	...
Day 2	2.93	7.03	3.13	2.10	-1.37	-0.89
Day 3	0	0	0	0	0	0
Day 4	2.61	7.27	3.71	2.28	-1.59	-0.99
Day 5	2.36	6.08	3.58	2.31	-1.54	-1.01
Day 6	2.74	8.05	4.41	2.24	-1.80	-0.98
Day 7	3.35	10.39	4.04	1.82	-1.69	-0.73

3.4. Time Delays

Given the remarkable capability of NIRCam's simultaneous observations at two wavelengths, a comparison of the 2.1 and 4.8 μm light curves was made to determine if there is a time delay. The cross-correlation of the light curves at these two wavelengths indicates for the first time that there is evidence for a delay in the 4.8 μm variable emission with respect to 2.1 μm in all observations. Figure 8 shows the cross-correlation of the light curves on 6 separate days showing time delays (Δt) labeled on each plot. The time delays range between 3 and 40 s.

Another characteristic of the observed flares is the presence of loops in the flux density versus spectral index plots. The loop feature is clearly noted in individual spectral index plots (bottom left panels of Figures 7–9 and 10–15 in Appendix C). The loop structures and time delays are modeled in Section 4.

3.5. Loop Structures

Figure 9 shows the variation of the spectral index as a function of F480M flux density for five subflares (left columns). Loop structures in these plots reveal the spectral index increase and decrease as a flare emission rises and decays. Additional loops are displayed in Figure 16,

Appendix C. In all these cases, the variations of the spectral index trace counterclockwise loops. The right panels show the light curves of individual flares, whereas the left panels display the 4.8 μm flux density of these events as a function of the spectral index. Each fluctuation shows a counterclockwise loop pattern as the flux density rises and decays. The pattern shows steepening of the spectral index as the 4.8 μm flux density rises followed by flattening of the spectral index as the flux density decreases.

4. Discussion

We have described some of the salient features, such as subminute and long-timescale quiescent variability, the 2 minute rise of the variable emission from Sgr A*, the time delays between 2.1 and 4.8 μm emission, and the dependence of the spectral index on the flux density of flare emission. In addition, we presented in seven epochs that Sgr A* is constantly fluctuating at NIR wavelengths with no evidence for a quiescent state, consistent with earlier ground-based and NICMOS observations (F. Yusef-Zadeh et al. 2009; G. C. Weldon et al. 2023). We had limited data to fit the flux distribution of Sgr A*, but our analysis indicates that two different populations of particles are needed to explain the flux distribution of Sgr A*. Two stochastic processes with LN distributions at 4.8 μm suggest that there are characteristic energy scales of the accelerating events for bright and faint fluxes. There are a number of new characteristics of flaring activity of Sgr A* as revealed in seven epochs of monitoring observations, as described in more detail below.

4.1. The Origin of Loop Diagrams and Time Delays

The characteristic loop structure that individual flares exhibit in the spectral index versus 2.1 μm flux plots in Figure 9 (see also Figures 10–15) occurs because at a given flux level, the spectral index of the falling part of the light curve is steeper than during the rise. This steepening is suggestive of

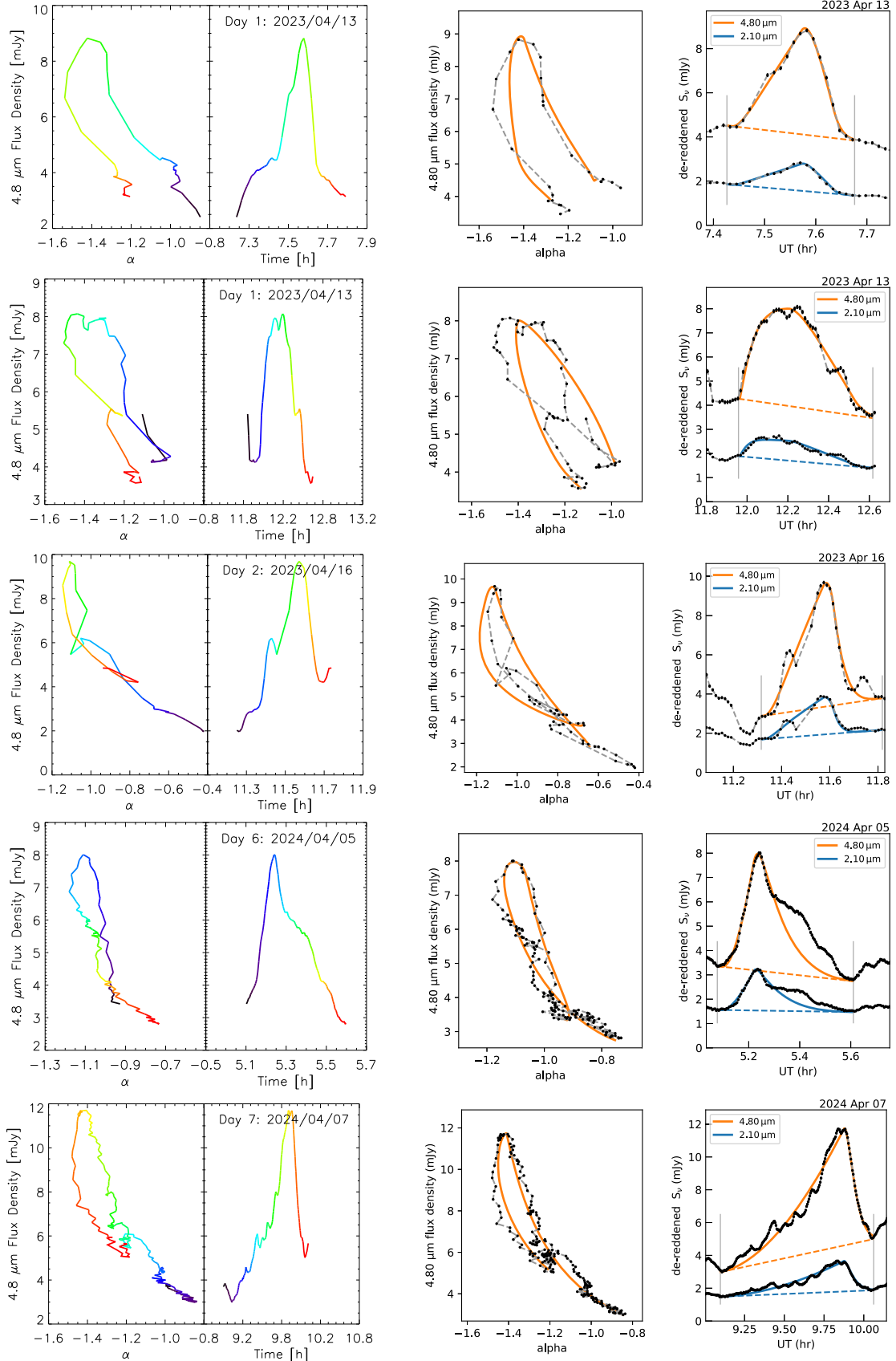


Figure 9. Left two columns: the variation of the spectral index as a function of F480M flux density is shown for five flares. The colors denote time. The variations of the spectral index trace counterclockwise loops. Right two columns: the modeled time delays and loop diagrams are interpreted to be due to synchrotron cooling, as the $4.8 \mu\text{m}$ emission lags in time behind the $2.1 \mu\text{m}$ emission. These fits provide the physical characteristics of individual flares (see Table 7).

Table 7
Flare Models

Date	UT ₀ (hr)	$S_{4.8}$ (mJy)	Δ_1 (s)	β_1	Δ_2 (s)	β_2	E_c (MeV)	B (G)	r_{\min}/r_g	$n_{e,\max}$ (cm ⁻³)
2023 Apr 13	7.44	4.83	489	0.98	220	0.92	424	92.7	0.32	5.21×10^5
2023 Apr 13	11.96	4.04	841	0.05	1154	0.95	537	38.3	0.83	0.57×10^4
2023 Apr 16	11.33	6.31	871	0.83	147	0.51	719	48.0	0.74	1.01×10^4
2024 Apr 5	5.09	4.80	455	1.53	165	4.00	736	88.5	0.33	4.64×10^5
2024 Apr 7	9.10	7.13	2798	1.83	1036	4.56	489	72.5	0.48	2.82×10^4

synchrotron cooling. The loop structures presented in Figure 9 are simpler to model because there are not many low-level fluctuations; thus, they are easier to identify. To explore this, we adopt a model in which electrons are injected into the source region with an E^{-2} spectrum and upper cutoff energy E_c ; the injected electrons subsequently suffer synchrotron losses in a constant magnetic field B . Injection commences, peaks, and ends at times t_0 , t_1 , and t_2 , respectively, with the injection rate rising as $(t - t_0)^{\beta_1}$ for $t_0 < t < t_1$ and declining as $(t_2 - t)^{\beta_2}$ for $t_1 < t < t_2$ (described in detail in Appendix D). The evolution of the electron population and the resultant synchrotron emission at 2.1 and 4.8 μm are then computed. Note that as the synchrotron emission is optically thin, the results depend only on the total number of electrons and their energy distribution, not on the size of the region, so this does not enter as a parameter.

We apply this model to five typical flares displayed in Figure 9 (left two panels). A linear baseline is subtracted from each flare, and the model light curves are fit to the residual light curves in the two IR bands. The observed light curves and best-fit model are compared in the left and right pairs of panels of Figure 9. The synchrotron emission at 4.80 and 2.10 μm from the evolving, age-stratified electron population reproduces the observed light curves quite well. Table 7 lists the parameters of the best-fit model in each case. The fits require a variety of injection rate shapes: the rise may be convex or concave, and the ratio of the time intervals for the rise and fall varies between 4 and 0.5. The inferred magnetic field strengths are in the range 38–92 G, consistent with the field strength in GRMHD simulations of the inner accretion flow (S. M. Ressler et al. 2020b, 2020a). The source size cannot be directly determined because the emission is optically thin, but if magnetic reconnection is responsible for powering the flare, then one expects that the source volume encloses magnetic energy of order a few times the energy dumped into the particles and subsequently radiated away, i.e., $E \approx 10^{37.5}$ erg. This implies a radius of a few times $\sim(8\pi E/B^2)^{1/3} \approx 0.5 r_g$.

4.2. The Origin of Two Components of the NIR Flux

The piecewise linear form of the flux–flux plots and the dual-component flux histograms indicate that there are two different processes contributing to the NIR variability. The first is a faint, continual flickering with $S(2.1 \mu\text{m}) \lesssim 3 \text{ mJy}$ and a steep spectral index $\alpha \sim -1.6$. The second, bright component consists of isolated flares with $\alpha \sim -0.85$ and $S(2.1 \mu\text{m}) \gtrsim 3 \text{ mJy}$.

A notable feature of our observations is that the qualitative appearance of the NIR light curves varies from day to day (see, e.g., the upper and lower panels of Figure 2). The emission underlying the bright flares secularly increases over the course of the observations on the first and final days. This is reflected

in the piecewise linear fits to the flux–flux plots on individual days (see Table 7), with the transition flux S_0 at 2.1 μm varying between about 2.4 and 4.3 mJy. Notably, the spectral index of the faint component only varies from -1.4 to -1.8 between the different epochs, consistent with electron power laws in the range $E^{-3.8}$ – $E^{-4.6}$. The flaring component also shows day-to-day variations: the spectral index varies between -0.63 and -1 (see Table 7). In addition, the flares on the final 2 days have notably larger amplitudes than the earlier days.

A plausible scenario is that the faint component is the synchrotron emission from a high-energy power-law tail (typically $\sim E^{-4.2}$) of the electron population in the inner accretion flow, and that this is moderated by the turbulent fluctuations in density and magnetic field strength (e.g., A. A. Grigorian & J. Dexter 2024). This implies that the accretion flow evolves significantly on ~ 10 hr timescales, as is apparent in many GRMHD simulations of Sgr A*. Our data suggest that the bright flare does not occur independently of the fainter variations, suggesting that nonthermal electrons are accelerated by occasional reconnection events within the bulk of the accretion flow (e.g., N. Scepi et al. 2022; I. Dimitropoulos et al. 2024; A. A. Grigorian & J. Dexter 2024) or, alternatively, from reconnection-driven ejection of plasmoids out of the disk plane (e.g., N. Aimar et al. 2023).

5. Summary

Simultaneous observations at two NIR wavelengths in seven epochs have accurately characterized the IR flare's spectral evolution. This tracks the evolution of the accelerated electron spectrum and has yielded information about the particle acceleration process and the subsequent cooling of the highest-energy particles. The additional information of detecting a flaring event at two wavelengths has provided estimates of the magnetic field strength and electron density of hot spots in the accretion flow. Our findings include the following.

1. Many measurements have found an LN or a power law or a combination of an LN and a power law in the past. Our data are not consistent with a single LN or tailed LN. The result shows the presence of a bright component that is distinct from the fainter component, suggesting two states described by two LN distributions for the faint and bright variability of Sgr A* (K. Dodds-Eden et al. 2009)
2. The power spectrum of the NIR variability follows a red-noise process with an index that varies in each epoch ranging between -3.57 and -2.70 . Across the 7 days, the power-law indices have mean values of -3.0 ± 0.3 at 2.1 μm and -3.0 ± 0.4 at 4.8 μm . The power spectra break, where the red noise turns to white noise, at frequencies ranging between 0.0060 and 0.0247 minute⁻¹, corresponding to 166 and 40 minutes, respectively. After the

removal of the white noise at high frequencies, we note that the highest frequencies are estimated between 0.45 and 2.34 minute⁻¹, corresponding to timescales of ~ 2.2 and 0.43 minute, respectively.

3. Reaching the white-noise level at high frequencies implies that a faster sampling rate cannot reveal the power law at high frequencies because shorter exposures have insufficient sensitivity for precise flux density measurements. Investigation of the intrinsic variability at higher frequencies might be possible by using wide-band filters rather than medium-band filters. Longer-wavelength observations (where Sgr A* is brighter) could also help, but confusion may be more of an issue with the lower angular resolution.
4. There is evidence of an intensity gradient showing flux density variation by a factor of 2 in ≤ 2 minutes. This suggests that the variability is arising from a small region of the accretion flow on a scale of a few gravitational radii or less.
5. A trend that we note in multiple flares is that subflares become increasingly stronger on the rising and/or the falling sides of flaring events. If the subflares and flares are physically associated with each other, then the subflares are precursors of bright flares.
6. The light curves also show pedestal emission with amplitudes that vary between each epoch, suggesting that there is long-term variability of Sgr A* on daily, monthly, and yearly timescales. The pedestal is varying roughly by a factor of 2 over seven epochs of observations.
7. The flux density histogram suggests two populations of faint and bright emission with two peaks near 2–3 and 10 mJy at 2.1 and 4.8 μm , respectively.
8. We note an anticorrelation of the spectral index with brightness (up to a limit) before it changes and shows a shallower spectral index with increasing brightness. The spectral index eventually saturates with increasing brightness with values close to $\alpha \sim -1$.
9. The cross-correlation of the light curves at 2.1 and 4.8 μm shows a systematic few-second delay in the 4.8 μm variable emission with respect to that of 2.1 μm in all observations. Another characteristic of the observed flares is the presence of loops in the flux density versus spectral index plots. The loop feature is noted in individual spectral index plots and is a loop pattern revealing the spectral index increase and decrease as a flare emission rises and decays.
10. The power spectrum shows no evidence of periodicity, but there is evidence of turnover at low frequencies in all of our observations. If the power spectrum did not turn over at low frequencies, the slow variations in the pedestal would be larger than the flares.
11. We suggested that the frequent low-amplitude variability arises from a high-energy power-law tail of the electron population in the accretion flow, with the fluctuations arising due to bright spots where turbulent motion or convection has temporarily compressed the plasma. The less common bright flares may be due to occasional magnetic reconnection events in the flow, as has been suggested by several authors (see the discussion Section 4.2).
12. We determine the spectral index of each component, and the power spectra represent observational signatures that models of these events need to reproduce. In addition, models of the bright flares must be able to explain the short rise time of bright flare events (i.e., ~ 2 minutes) and the duration and spectral “loop” evolution that is consistently found in our measurements.
13. A trend that we note is that subflares are precursors to strong flares. We noted some apparent qualitative behavior that we were unable to quantify: smaller subflares appear to be precursors to strong flares, and the underlying pedestal emission is often increased immediately after a flare. These may be signatures of correlated activity: for example, the emission from bright flares may feed back on the accretion flow to enhance its NIR emission.

Acknowledgments

Some of the data presented in this Letter were obtained from the Mikulski Archive for Space Telescopes (MAST) at the Space Telescope Science Institute. All the JWST data used in this Letter can be found in MAST: doi:[10.17909/0z7e-gf46](https://doi.org/10.17909/0z7e-gf46). This work is based on observations made with the NASA/ESA/CSA James Webb Space Telescope. The data were obtained from the Mikulski Archive for Space Telescopes at the Space Telescope Science Institute, which is operated by the Association of Universities for Research in Astronomy, Inc., under NASA contract NAS 5-03127 for JWST. These observations are associated with NASA’s JWST-2235 and JWST-3559 programs. This Letter makes use of the following ALMA data: ADS/JAO.ALMA#2022.A.00029.S. ALMA is a partnership of ESO (representing its member states), NSF (USA), and NINS (Japan), together with NRC (Canada), NSTC and ASIAA (Taiwan), and KASI (Republic of Korea), in cooperation with the Republic of Chile. The Joint ALMA Observatory is operated by ESO, AUI/NRAO and NAOJ. This work is also partially supported by the grant AST-2305857 from the NSF. The National Radio Astronomy Observatory is a facility of the National Science Foundation operated under cooperative agreement by Associated Universities, Inc. Work by R.G.A. was supported by NASA under award number 80GSFC24M0006. Lastly, we thank S. Markoff, G. Bower, D. Haggard, and K. Hada for useful comments.

Software: IDLASTRO (W. B. Landsman [1995](#))

Appendix A Polynomial Fits to Pedestal Emission

Fourth order was chosen purely subjectively in order to allow more freedom for variation (changes in slope) during the interval while avoiding too much freedom that would allow the pedestal to start tracing the behavior of the larger flaring events. On each day of observations, a lower envelope $f'(t)$ was fit to the light curves $f(t)$ using a fourth-degree polynomial. The choice of degree was subjective, with the intent to allow more freedom for variation than a simple linear fit while avoiding too much freedom that would allow the fit to start tracing the behavior of the larger flaring events. The exact procedure used

is that the polynomial fit is specified by

$$f'(t) = a_0 + \sum_{i=1}^4 a_i t^i, \quad (\text{A1})$$

with the constraint that

$$a_0 = \min \left(f(t) - \sum_{i=1}^4 a_i t^i \right) \quad (\text{A2})$$

such that

$$f(t) - f'(t) \geq 0. \quad (\text{A3})$$

The IDL procedure MPFITFUN (C. B. Markwardt 2009) was used to optimize the parameters $[a_1, a_2, a_3, a_4]$ to minimize χ^2 .

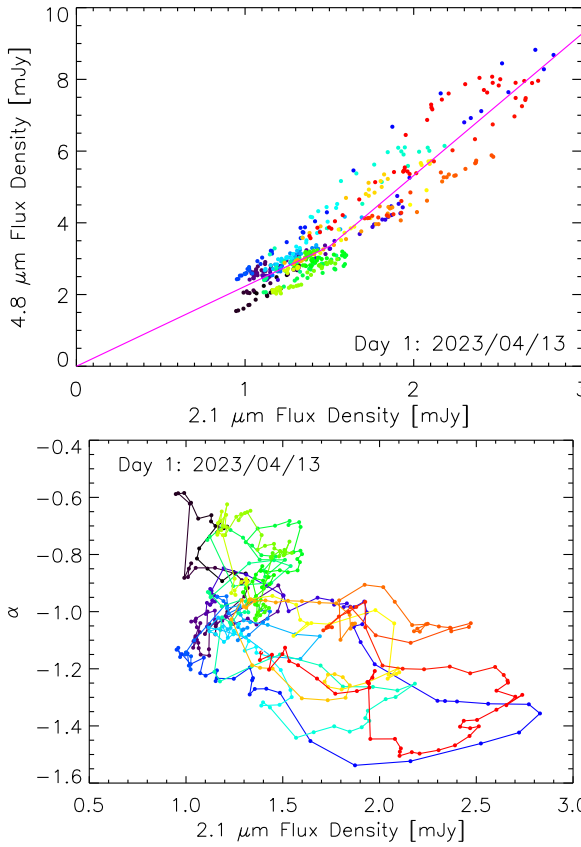
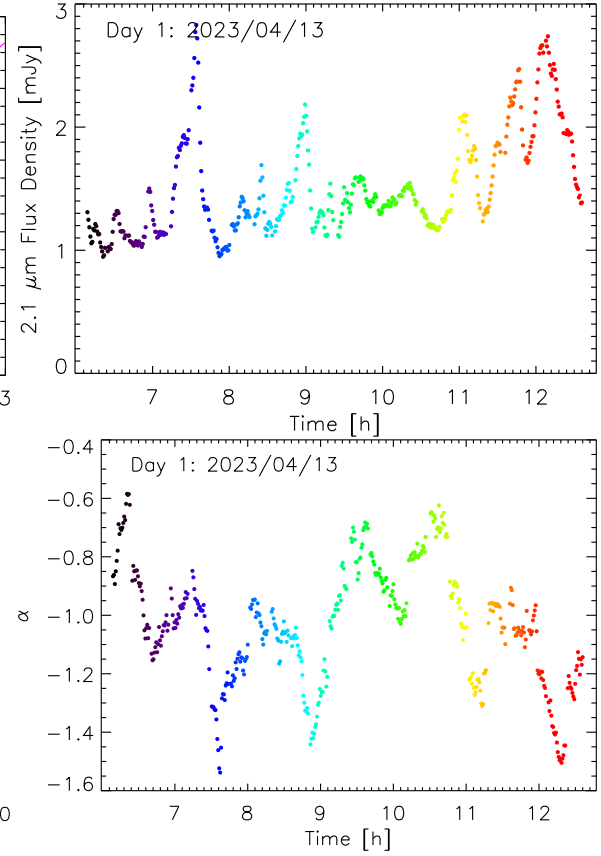


Figure 10. Similar to Figure 7, where data for all days are shown. The top left panel shows the colored variation of the $4.8 \mu\text{m}$ flux against the $2.1 \mu\text{m}$ flux density. The top right panel shows light curves of Sgr A* in color at $2.1 \mu\text{m}$. The bottom left panel shows the spectral index of Sgr A* in color as a function of $2.1 \mu\text{m}$ flux density. The bottom right panel shows the spectral index as a function of each time in color.

Appendix B The Spectral Index versus the Flux Density for Individual Days

Figures 10–15 are very similar to Figure 7, showing four panels describing the correlation and anticorrelation of the spectral index versus flux density for days 1–7 (excluding day 3). These figures show that the slope of the faint flux is steeper than that of the bright flux, suggesting two different populations with different spectral indices. For each day of observation, the four panels display the flux density at $2.1 \mu\text{m}$ versus $4.8 \mu\text{m}$, the colored light curves, the spectral index as a function of $2.1 \mu\text{m}$, and the colored spectral index as a function of time. Similar trends noted for combined data can also be seen for individual data sets.



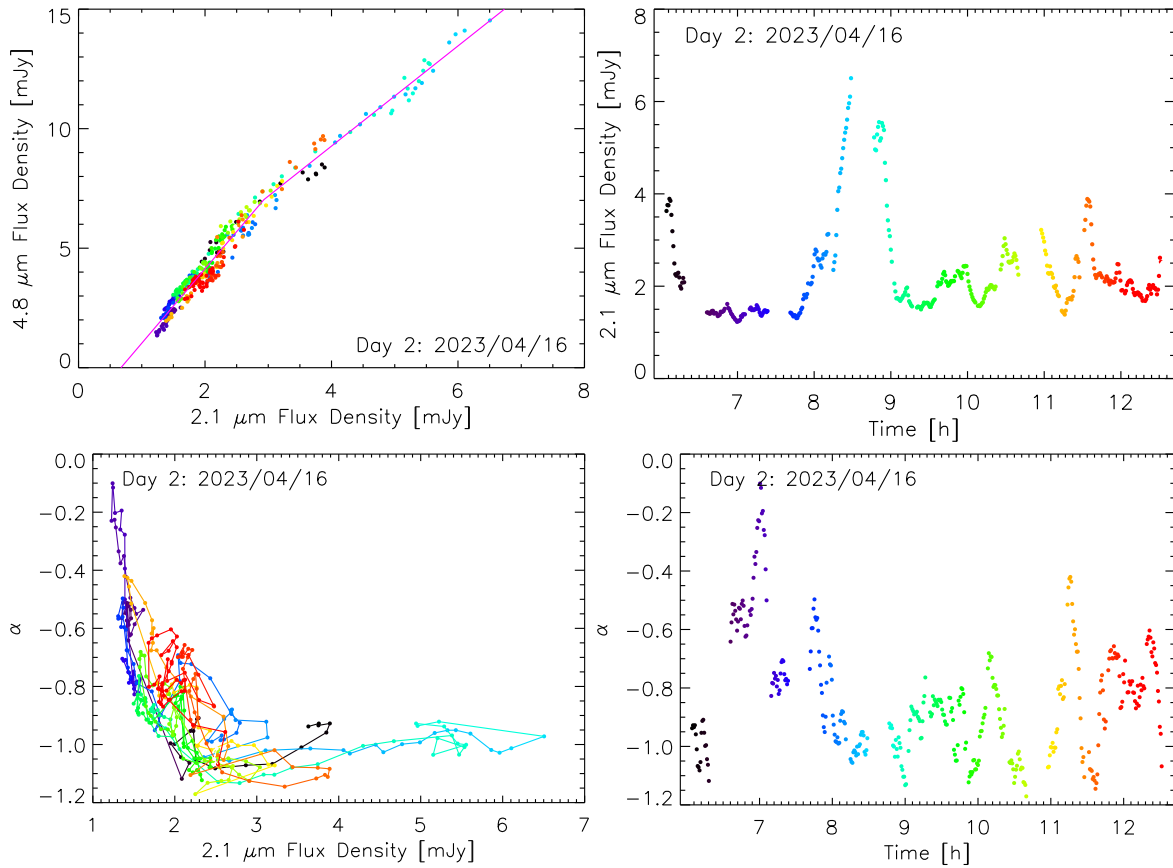


Figure 11. Same as Figure 7 but showing day 2 data.

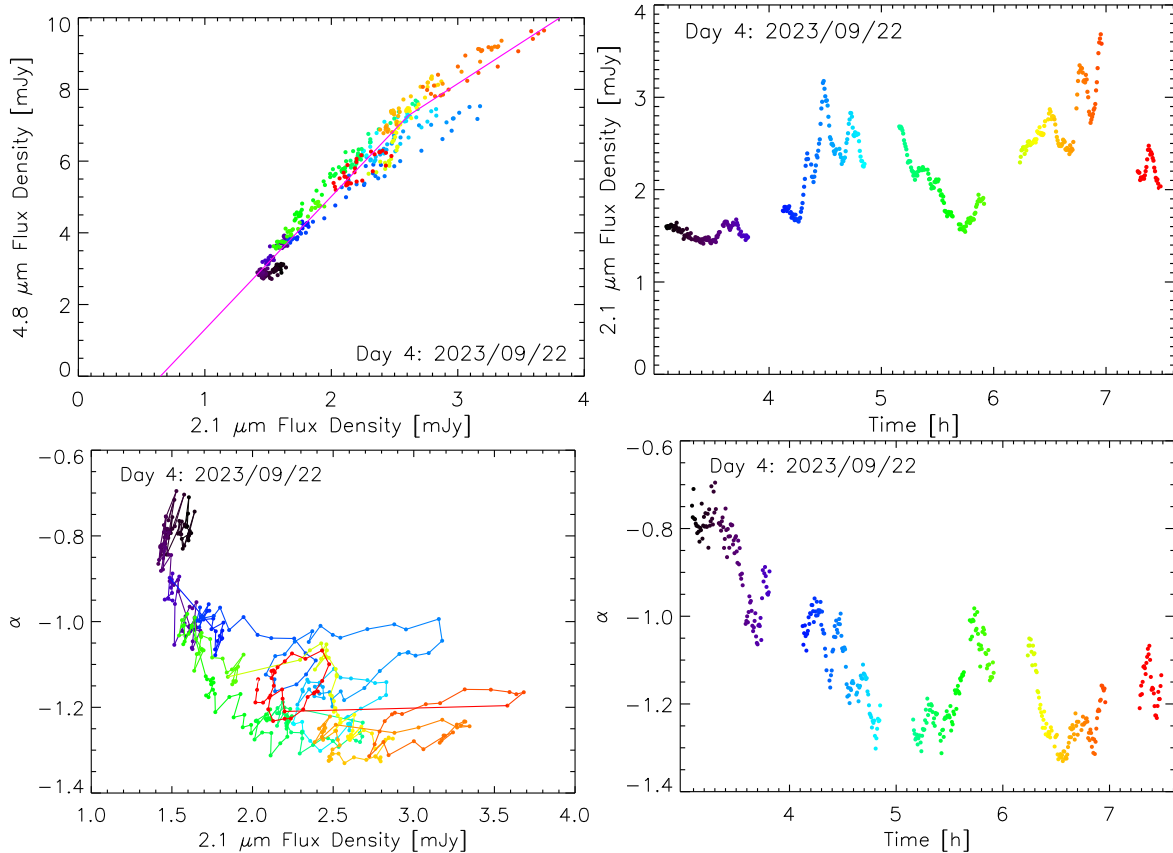


Figure 12. Same as Figure 7 but showing day 4 data.

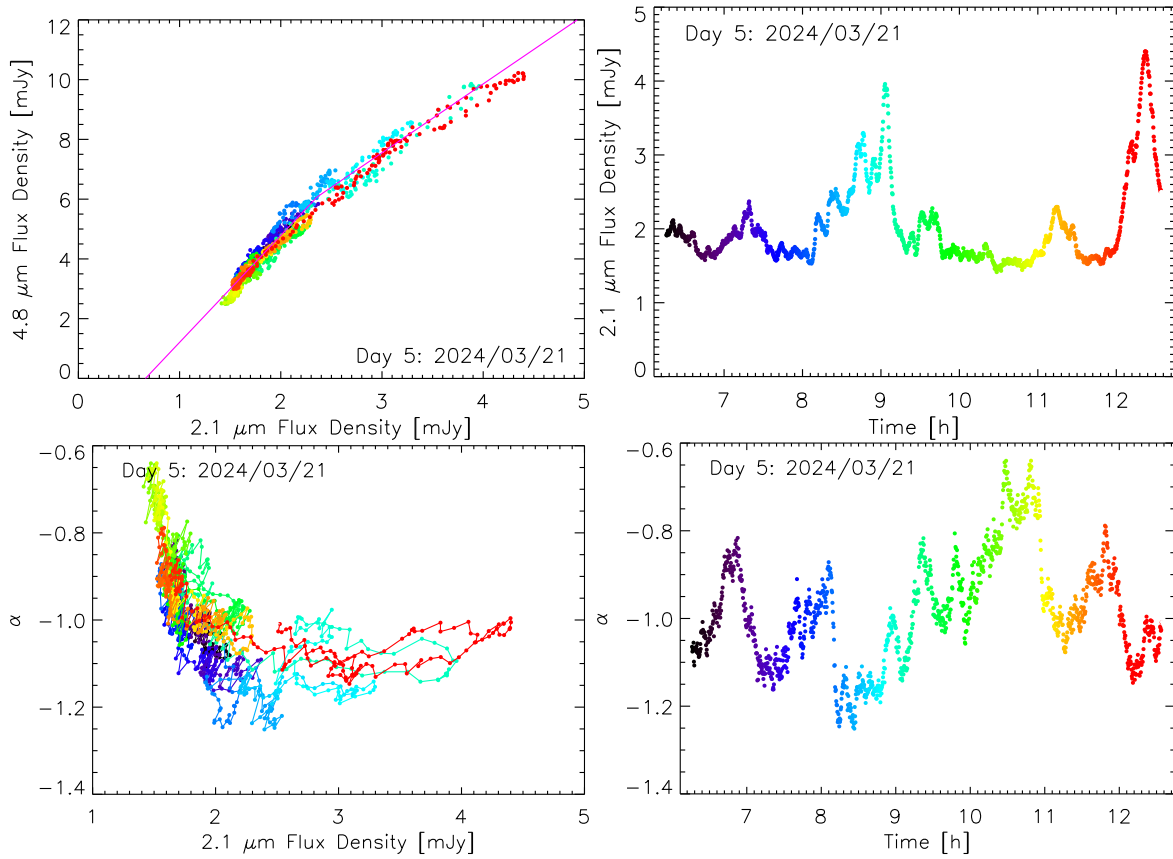


Figure 13. Same as Figure 7 but showing day 5 data.

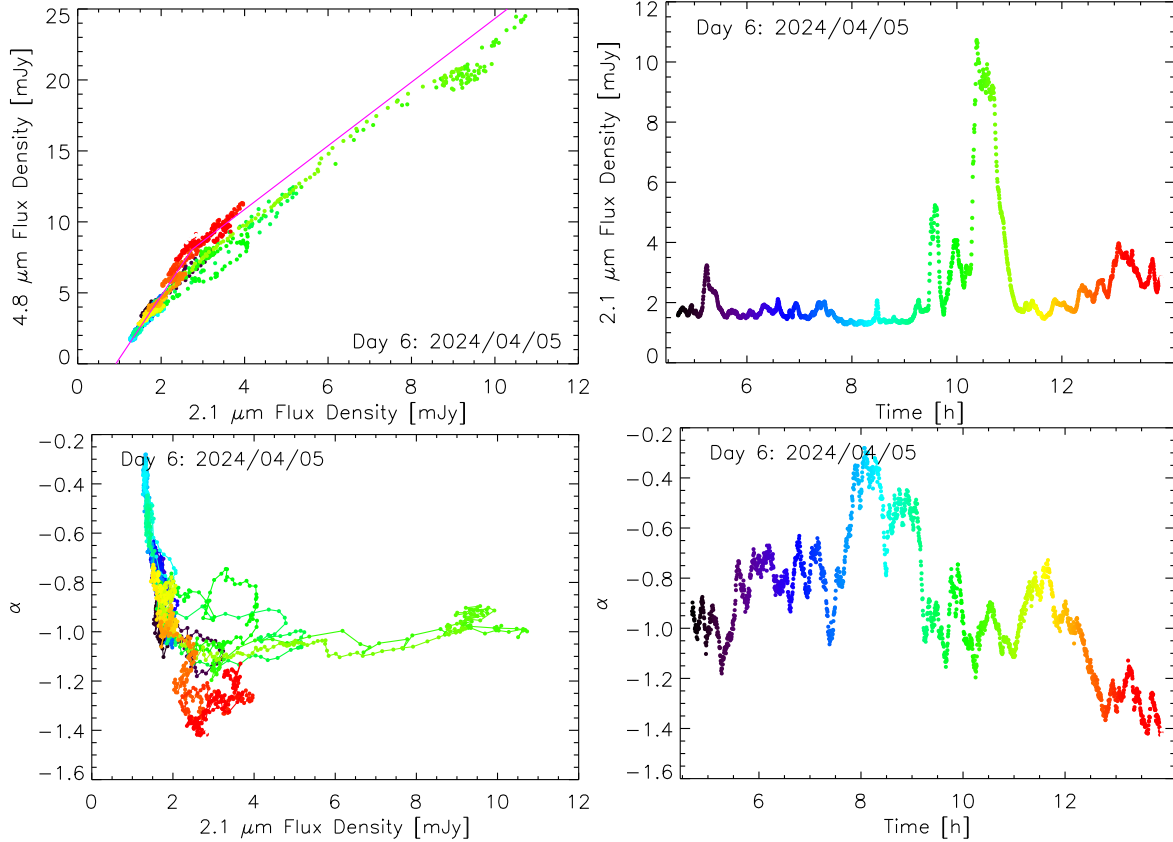


Figure 14. Same as Figure 7 but showing day 6 data.

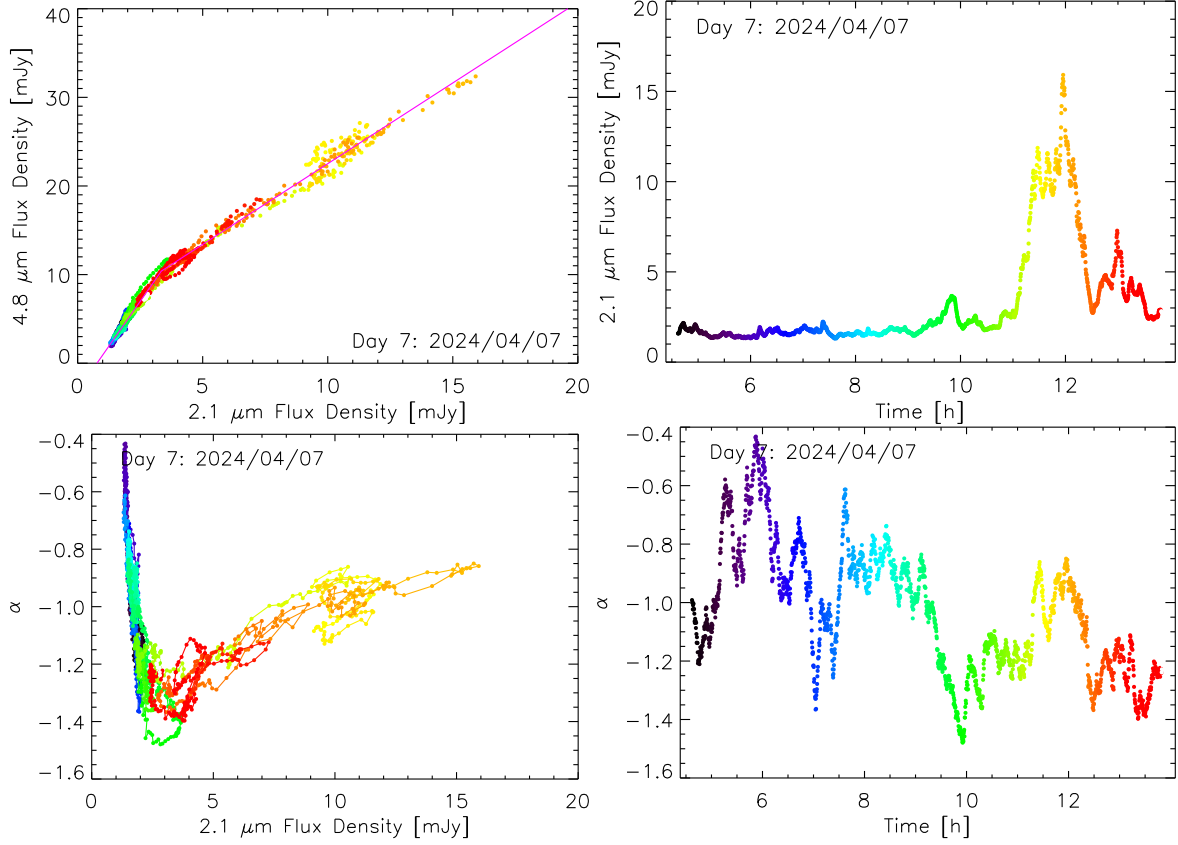


Figure 15. Same as Figure 7 but showing day 7 data.

Appendix C Complex Loop Structures

Loop structures reveal that the spectral index increases and decreases as a flare emission rises and decays. Figure 16 shows the variation of the spectral index as a function of F480M flux density for six complex subflares. In all these cases, the variations of the spectral index trace counterclockwise loops. The right panels show the light curves of individual colored flares and subflares on days 4–7. We note that low-level

fluctuations or subflares are superimposed on these flares and thus harder to model. The left panels display the $4.8\text{ }\mu\text{m}$ flux density of these events as a function of the spectral index. Each fluctuation shows a counterclockwise loop pattern as the flux density rises and decays. The pattern shows steepening of the spectral index as the $4.8\text{ }\mu\text{m}$ flux density rises followed by flattening of the spectral index as the flux density decreases. There are counterclockwise loops corresponding to each subflare.

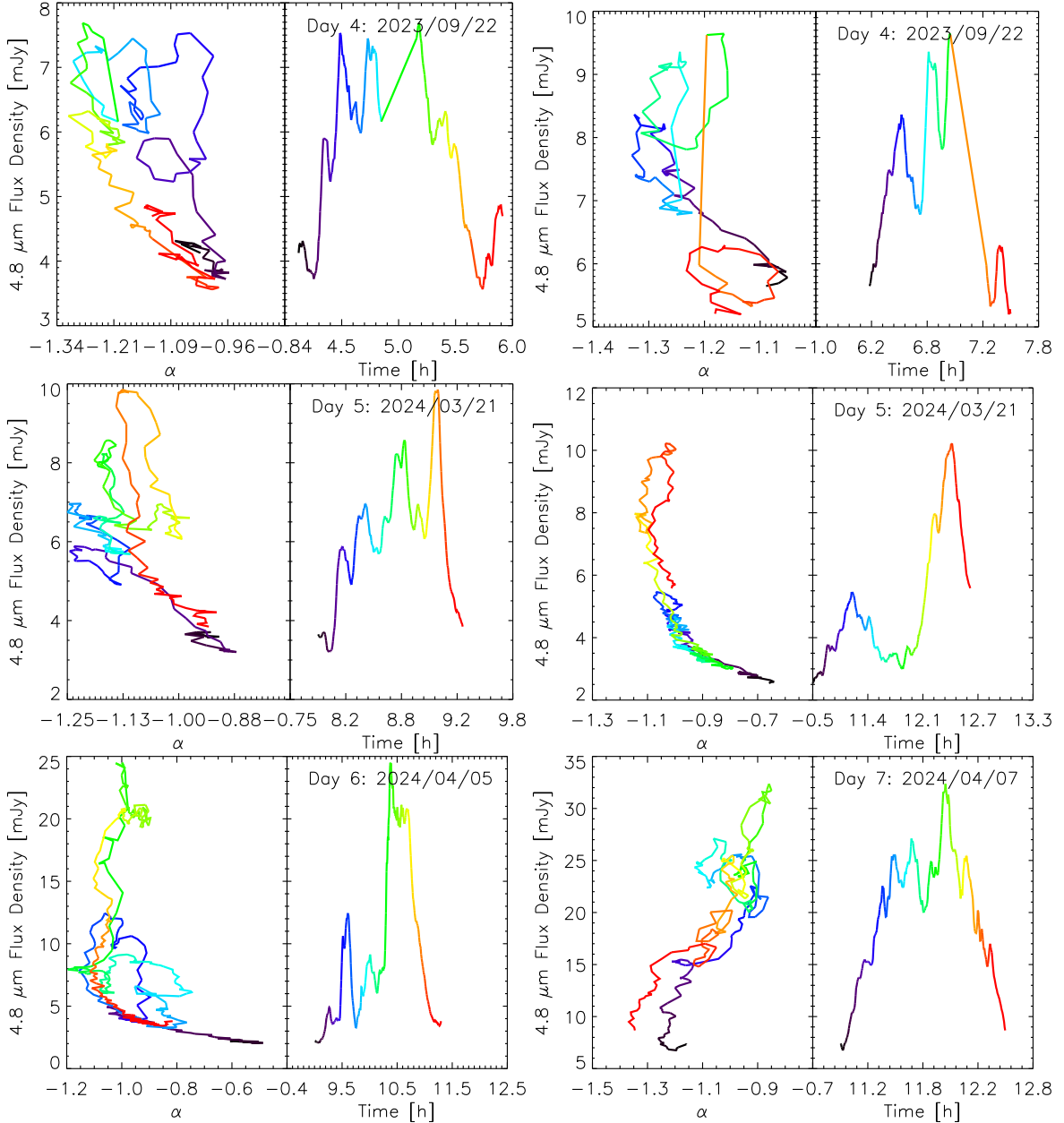


Figure 16. Similar to Figure 9 (left two columns) except that more complex flares with multiple subflares are selected.

Appendix D Electron Population in an Evolving Injection Rate and Magnetic Field

Here we derive expressions for the electron population in a region given an evolving injection rate $Q(E, t)$ (electrons $\text{cm}^{-3} \text{erg}^{-1} \text{s}^{-1}$) and subject to synchrotron losses in a magnetic field $B(t)$. We start by considering the energy lost by a single electron; from this, we derive how a population evolves due to synchrotron losses.

An ultrarelativistic electron with energy E suffers synchrotron losses at a rate

$$\frac{dE}{dt} = -bB^2E^2, \quad (\text{D1})$$

where

$$b = \frac{4e^3}{9m_e^4 c^5}. \quad (\text{D2})$$

For simplicity, we have neglected the dispersion in loss rates due to different pitch angles and adopted the loss rate averaged over an isotropic pitch-angle distribution. Thus, at time t , an electron of age τ with energy E was injected at time $t - \tau$ with initial energy E_0 , where

$$\frac{1}{E_0} = \frac{1}{E} - b \int_0^\tau [B(t - \tau')]^2 d\tau'. \quad (\text{D3})$$

Now consider a cohort of electrons, $N(E, t)$ (electrons erg^{-1}), that were injected at time $t - \tau$ and now have age τ . The

electrons that were injected with initial energy in an interval $[E_0, E_0 + dE_0]$ are now in the interval $[E, E + dE]$, where E and E_0 are given by Equation (D3). Thus, the initial and present populations are related via $N_0(E_0, t - \tau)dE_0 = N(E, t)dE$, where $dE_0/E_0^2 = dE/E^2$ and so the initial and current populations are related via $N(E, t) = E_0^2 N(E_0, t - \tau)/E^2$.

For injection rate $Q(E, t)$, the initial population of electrons with ages in the interval $[\tau, \tau + d\tau]$ is $N(E_0) = Q(E_0, t - \tau)d\tau$, and the contribution to the population at time t is $E_0^2 Q(E_0, t - \tau) d\tau/E^2$. The net population at time t is obtained by integrating over all ages, i.e.,

$$N(E, t) = \frac{1}{E^2} \int_0^\infty E_0^2 Q(E_0, t - \tau) d\tau. \quad (\text{D4})$$

Note that E_0 depends on τ via Equation (D3).

The synchrotron luminosity of the population is, assuming an isotropic electron pitch-angle distribution and averaging over an isotropic distribution of field orientations,

$$L_\nu = \frac{\sqrt{3} e^3 B}{m_e c^2} \int_0^\infty N(E, t) G(x) dE, \quad (\text{D5})$$

where

$$x = \frac{4\pi m_e c \nu}{3eB} \left(\frac{E}{m_e c^2} \right)^{-2} \quad (\text{D6})$$

and $G(x)$ can be approximated to within 0.2% by

$$G(x) \approx \frac{1.808 x^{1/3}}{\sqrt{1 + 3.4 x^{2/3}}} \frac{1 + 2.21 x^{2/3} + 0.347 x^{4/3}}{1 + 1.353 x^{2/3} + 0.217 x^{4/3}}, \exp(-x) \quad (\text{D7})$$

$$R(t) = \begin{cases} \left(\frac{t - t_0}{t_1 - t_0} \right)^{\beta_1} & \text{if } t_0 < t < t_1, \\ \left(\frac{t_2 - t}{t_2 - t_1} \right)^{\beta_2} & \text{if } t_1 < t < t_2, \text{ or} \\ 0 & \text{otherwise.} \end{cases} \quad (\text{D8})$$

For simplicity, we assume that B is constant and adopt an injection rate

$$Q(E, t) = Q_0 R(t) \left(\frac{E}{E_1} \right)^{-p} \quad \text{for } E_1 < E < E_c \quad (\text{D9})$$

and 0 otherwise. We set $E_1 = 2$ MeV and $p = 2$ and treat the cutoff energy E_c as a free parameter. The injection envelope rises monotonically from 0 to 1 between $t = t_0$ and t_1 , then declines monotonically to 0 at $t = t_2$; β_1 and β_2 control the shape of the rise and fall.

Once the six free parameters— B , Q_0 , E_c , t_0 , t_1 , and t_2 —are specified, we compute the light curves $S_\nu(t) = L_\nu/(4\pi d^2)$ using Equation (D5) at 143 and 62.5 THz, i.e., the frequencies equivalent to 2.1 and 4.8 μm , respectively.

ORCID iDs

F. Yusef-Zadeh <https://orcid.org/0000-0001-8551-9220>
H. Bushouse <https://orcid.org/0000-0001-6664-7585>
R. G. Arendt <https://orcid.org/0000-0001-8403-8548>

M. Wardle <https://orcid.org/0000-0002-1737-0871>
J. M. Michail <https://orcid.org/0000-0003-3503-3446>
C. J. Chandler <https://orcid.org/0000-0002-7570-5596>

References

Aimar, N., Dmytriiev, A., Vincent, F. H., et al. 2023, *A&A*, **672**, A62
Bremer, M., Witzel, G., Eckart, A., et al. 2011, *A&A*, **532**, A26
Chatterjee, K., Markoff, S., Neilsen, J., et al. 2021, *MNRAS*, **507**, 5281
Dexter, J., Jiménez-Rosales, A., Ressler, S. M., et al. 2020, *MNRAS*, **494**, 4168
Dexter, J., Kelly, B., Bower, G. C., et al. 2014, *MNRAS*, **442**, 2797
Dimitropoulos, I., Nathanail, A., Petropoulou, M., Contopoulos, I., & Fromm, C. M. 2024, arXiv:2407.14312
Do, T., Ghez, A. M., Morris, M. R., et al. 2009, *ApJ*, **691**, 1021
Dodds-Eden, K., Porquet, D., Trap, G., et al. 2009, *ApJ*, **698**, 676
Event Horizon Telescope Collaboration, Akiyama, K., Alberdi, A., et al. 2022, *ApJL*, **930**, L12
Eckart, A., Schödel, R., García-Marín, M., et al. 2008, *A&A*, **492**, 337
Eisenhauer, F., Genzel, R., Alexander, T., et al. 2005, *ApJ*, **628**, 246
Fazio, G. G., Hora, J. L., Witzel, G., et al. 2018, *ApJ*, **864**, 58
Genzel, R., Schödel, R., Ott, T., et al. 2003, *Natur*, **425**, 934
Ghez, A. M., Hornstein, S. D., Lu, J. R., et al. 2005, *ApJ*, **635**, 1087
Gillessen, S., Eisenhauer, F., Quataert, E., et al. 2006, *ApJL*, **640**, L163
Gillessen, S., Plewa, P. M., Eisenhauer, F., et al. 2017, *ApJ*, **837**, 30
Goldston, J. E., Quataert, E., & Igumenshchev, I. V. 2005, *ApJ*, **621**, 785
Gordon, D., de Witt, A., & Jacobs, C. S. 2023, *AJ*, **165**, 49
GRAVITY Collaboration, Abuter, R., Amorim, A., Bauböck, M., et al. 2018, *A&A*, **618**, L10
GRAVITY Collaboration, Abuter, R., Amorim, A., Bauböck, M., et al. 2020, *A&A*, **638**, A2
Grigorian, A. A., & Dexter, J. 2024, *MNRAS*, **530**, 1563
Hora, J. L., Witzel, G., Ashby, M. L. N., et al. 2014, *ApJ*, **793**, 120
Hornstein, S. D., Matthews, K., Ghez, A. M., et al. 2007, *ApJ*, **667**, 900
Krabbe, A., Iserlohe, C., Larkin, J. E., et al. 2006, *ApJL*, **642**, L145
Landsman, W. B. 1995, in ASP Conf. Ser. 77, Astronomical Data Analysis Software and Systems IV, ed. R. A. Shaw, H. E. Payne, & J. J. E. Hayes (San Francisco, CA: ASP), 437
Markwardt, C. B. 2009, in ASP Conf. Ser. 411, Astronomical Data Analysis Software and Systems XVIII, ed. D. A. Bohlender, D. Durand, & P. Dowler (San Francisco, CA: ASP), 251
Meyer, L., Do, T., Ghez, A., et al. 2009, *ApJL*, **694**, L87
Michail, J. M., Yusef-Zadeh, F., Wardle, M., et al. 2024, *ApJ*, **971**, 52
Michail, J. M., Wardle, M., Yusef-Zadeh, F., & Kunneriath, D. 2021, *ApJ*, **923**, 54
Moscibrodzka, M., & Falcke, H. 2013, *A&A*, **559**, L3
Mossoux, E., Grosso, N., Bushouse, H., et al. 2016, *A&A*, **589**, A116
Neilsen, J., Nowak, M. A., Gammie, C., et al. 2013, *ApJ*, **774**, 42
Paugnat, H., Do, T., Gautam, A. K., et al. 2024, *ApJ*, **977**, 228
Ponti, G., George, E., Scaringi, S., et al. 2017, *MNRAS*, **468**, 2447
Quataert, E. 2004, *ApJ*, **613**, 322
Ressler, S. M., Quataert, E., & Stone, J. M. 2020a, *MNRAS*, **492**, 3272
Ressler, S. M., White, C. J., & Quataert, E. 2023, *MNRAS*, **521**, 4277
Ressler, S. M., White, C. J., Quataert, E., et al. 2020b, *ApJL*, **896**, L6
Rieke, M. J., Kelly, D. M., Misselt, K., et al. 2023, *PASP*, **135**, 028001
Scepi, N., Dexter, J., & Begelman, M. C. 2022, *MNRAS*, **511**, 3536
Schödel, R., Morris, M. R., Muzic, K., et al. 2011, *A&A*, **532**, A83
Trap, G., Goldwurm, A., Dodds-Eden, K., et al. 2011, *A&A*, **528**, A140
von Fellenberg, S. D., Witzel, G., Bauböck, M., et al. 2024, *A&A*, **688**, L12
Wang, Q., & Moerner, W. E. 2015, *PNAS*, **112**, 13880
Weldon, G. C., Do, T., Witzel, G., et al. 2023, *ApJL*, **954**, L33
Wielgus, M., Marchili, N., Martí-Vidal, I., et al. 2022, *ApJL*, **930**, L19
Witzel, G., Ghez, A. M., Morris, M. R., et al. 2014, *ApJL*, **796**, L8
Witzel, G., Martinez, G., Hora, J., et al. 2018, *ApJ*, **863**, 15
Witzel, G., Martinez, G., Willner, S. P., et al. 2021, *ApJ*, **917**, 73
Yuan, F., & Narayan, R. 2014, *ARA&A*, **52**, 529
Yuan, F., Quataert, E., & Narayan, R. 2003, *ApJ*, **598**, 301
Yusef-Zadeh, F., Bushouse, H., Dowell, C. D., et al. 2006, *ApJ*, **644**, 198
Yusef-Zadeh, F., Bushouse, H., Witzel, G., et al. 2009, *ApJ*, **706**, 348
Yusef-Zadeh, F., Roberts, D., Wardle, M., Heinke, C. O., & Bower, G. C. 2006, *ApJ*, **650**, 189